Secure Communication through Free-space Channel Using Quantum Illumination

by

Jiwon Yune

Submitted to the Department of Electrical Engineering and Computer Science
in partial fulfillment of the requirements for the degree of

Master of Engineering in Electrical Engineering and Computer Science

at the

MASSACHUSETTS INSTITUTE OF TECHNOLOGY

June 2014

Signature redacted

Author .....
Department of Electrical Engineering and Computer Science
May 27, 2014

Signature redacted

Certified by .....
Dr. Franco N. C. Wong
Senior Research Scientist
Thesis Supervisor

Signature redacted

Accepted by .....
Prof. Albert R. Meyer
Chairman, Master of Engineering Thesis Committee

Secure Communication through Free-space Channel Using Quantum Illumination

by

Jiwon Yune

Submitted to the Department of Electrical Engineering and Computer Science
on May 23, 2014, in partial fulfillment of the
requirements for the degree of
Master of Engineering in Electrical Engineering and Computer Science

Abstract

Secure communication based on quantum illumination (QI) provides high-speed direct communication in the presence of loss and noise and is secure against passive eavesdropping. Recently, the QI based communication protocol has been demonstrated in a fiber channel. In this thesis, we extend the QI secure communication protocol to a free-space propagation channel. Unlike a fiber channel, a free-space channel is susceptible to air turbulence. Because a single spatial mode of light is essential in the QI protocol, if the beam path is affected by air turbulence, the power and phase may fluctuate, which can affect the interferometric measurement performance of QI. In order to fix this issue, we have designed and implemented a servo system to stabilize the coupling of the free-space propagating beam into a single-mode fiber. The servo system utilizes the X and Y tilts of a single piezoelectrically driven mirror mount, together with a quadrant detector, to stabilize the beam location at the collimation optics of the free-space path. To demonstrate the QI-based secure communication with a free-space path, we use a heat source to simulate air turbulence. We have demonstrated that the free-space secure communication using quantum illumination is still possible in an environment with air fluctuation, by using a servo system to counteract the deleterious effect the effect from air turbulence. Without air tubulence, we have demonstrated that $\mathrm{BER}_A \approx 5.8 \times 10^{-4}$ for a free-space channel implemented in the Bob-to-Alice path or Alice-to-Bob path with $\mathrm{N}_S \approx 5.6 \times 10^{-4}$. When we introduce a heat source at a known setting, the effective attenuation $\overline{h}$ for the Bob-to-Alice or Alice-to-Bob channel transmissivity is found to be 0.63. Without the servo system, BER_A drops to 2.40×10^{-4} and 9.8×10^{-3} for the free-space Bob-to-Alice and Alice-to-Bob channels, respectively, for the same amount of N_S. With both heat source and the servo system on, we have successfully operated the QI-based secure communication protocol and obtained the same level of Alice's BER as that without the heat source.

Thesis Supervisor: Dr. Franco N.C. Wong
Title: Senior Research Scientist

Acknowledgments

First of all, I would like to thank Dr. Franco Wong and Prof. Jeff Shapiro for giving me this opportunity to study one of the most interesting topics in quantum information science. Especially, I am verye grateful to Dr. Wong for his mentorship and patience. I would also like to thank Dr. Zheshen Zhang for providing so much educational support in the lab. They are the pioneers of this field, and I have truly learned a lot from them. I also want to thank Prof. Vladan Vuletic who triggered my interest in quantum science and had me as a research assistant at RLE when I was still a high school student. I'd also like to thank the members of Sigma Delta and KBL for their emotional support. I want to thank my parents for their unlimited and unconditional love. Because of them, everything I did was possible. Lastly, I am very thankful to the U.S. Office of Naval Research for funding and supporting this work.

Contents

1 Introduction **15**

2 Secure Communication Protocol **19**

2.1 Entanglement generation 20

2.2 Message Encoding 22

2.3 Noise Injection 23

2.4 Joint Measurement 23

2.5 Eavesdropping 24

2.6 Result of the Fiber Channel Communication 24

3 QI-based Secure Communication with a Free-space Link **31**

3.1 Free-space Channel Communication via Quantum Illumination 32

3.2 Fiber Coupling 34

3.3 Servo Loop Design 35

3.3.1 Quadrant Detector and Reader 36

3.3.2 Piezoelectric Adjusters and Drivers 38

3.3.3 Operational Modes 38

3.3.4 Feedback Signal Conditioning 39

3.3.5 Results 41

3.4 Path Matching 42

3.5 Part Numbers and Settings 42

4 Experimental Results **47**

4.1 Changes in the Experimental Parameter Values in the Free-space Communication 47
4.2 Results of the Free-space Communication 48
4.2.1 Analysis on the Bob-to-Alice Channel 49
4.2.2 Analysis on the Alice-to-Bob Channel 52
4.3 Further Experimental Optimization 55
4.4 Conclusion 56

Appendices **57**

A MATLAB Code for the free-space Alice-to-Bob Channel Analysis **59**

List of Figures

1-1 Basic schematic of quantum illumination. 16

2-1 Experimental setup with fiber channels. SPDC: spontaneous parametric downconverter; DM: dichroic mirror; C: fiber collimator; CWDM: coarse wavelength-division multiplexer; BS: beam splitter; Attn: attenuator; EDFA: erbium-doped fiber amplifier; DL: delay line; PC: polarization convtoller; PM: phase modulator; AAG: adjustable air gap; Pol: polarizer; DCF: dispersion-compensating fiber; DSF: dispersion-shifted fiber; TEC: thermo-electric cooler; OPA: optical parametric amplifier; D: photodetector. Figure reproduced from Ref. [9]. 19

2-2 Theoretical model for tQI-based secure communication. BPSK: binary phase-shift keying. Figure reproduced from Ref. [9]. 20

2-3 Plots of BER_A and BER_E as functions of source brightness N_S for 500 kbit/s communication. Blue-dotted line: BER_A for ideal OPA receiver; Blue solid line: BER_A for actual OPA receiver; Green-dotted line: BER_E for ideal receiver; Green solid line: BER_E for actual receiver. Error bars represent the experimental data collected with the parameter values in table 2.1. [9] 29

2-4 Trace of 25 bits of OPA receiver output (blue) and Bob's corresponding modulation waveform (red). [9] 30

3-1 Fiber channels between Alice and Bob. 32

3-2 Servo system design for the Alice-to-Bob free-space channel. For the experiment, we have set the following distances: 15 cm from Alice's collimator to air-turbulence zone; 80 cm from the piezo mirror to Bob's collimator; the total distance between Alice's and Bob's collimators is 1.2 m. Note that the figure is not drawn to scale. 33

3-3 Wavelength vs. transmission at 18° angle. 35

3-4 Block diagram of the servo loop system; red line symbolizes the light signal, and blue line symbolizes the electric signal; quad-detector: quadrant detector; QD reader: quandrant detector reader. 36

3-5 Schematic of quadrant detector 37

3-6 Change in angle as a function of the piezo control voltage. 38

3-7 Low-pass step filter circuit model. 40

3-8 Bode plot of low-pass step filter; R0 = 1 kΩ, R1 = 0.1 kΩ, R2 = 100 kΩ, and C1 = 10 μF. Note that the unit is in Hz and dB. 44

3-9 Time trace on the photodetector voltage for the open- and closed-loop modes 45

3-10 Comparison between open-loop and closed-loop responses. 46

4-1 Plots of BER_A and BER_E as functions of source brightness N_S for 500 kbit/s communication. Red solid line: BER_A measured with a PiN diode. Other curves are the same as in Fig. 2-3. 48

4-2 Plots of BER_A and BER_E as functions of source brightness N_S for 180 kbit/s communication when is replaced the Bob-to-Alice channel with a free-space channel. Blue-dotted line: BER_A for ideal OPA receiver; Blue solid line: BER_A for actual OPA receiver measured with a PiN diode; Red-dotted line: BER_E for ideal receiver. 50

4-3 The effect of heat on the free-space Bob-to-Alice channel. Black dashed line: calculated open-loop operation with heat (open circle at measured point); Blue solid line: calculated closed-loop operation with heat (filled diamond at measured point). 52

4-4 Plots of BER_A and BER_E as functions of source brightness N_S for 180 kbit/s communication when is replaced the Alice-to-Bob channel with a free-space channel. Blue-dotted line: BER_A for ideal OPA receiver; Blue solid line: BER_A for actual OPA receiver measured with a PiN diode; Red-dotted line: BER_E for ideal receiver. 53

4-5 The effect of heat on the free-space Alice-to-Bob channel. Black dashed line: open-loop operation with heat (open circle at measured point); Blue solid line: closed-loop operation with heat (filled diamond with measured point). 54

List of Tables

2.1 Experimentally-determined parameter values for the fiber communication channels [9]. 25

3.1 Table of the manufacturers and part numbers of the system components. 43

3.2 Table of the parameter values for the quadrant detector reader. . . . 43

4.1 Modifications in experimentally-determined parameter values for free-space QI-based communication. 49

Chapter 1

Introduction

Quantum illumination (QI) was first proposed by Seth Lloyd in 2008 [1]. He introduced a method to reduce the effective noise and detect the target of interest using quantum entanglement in the presence of high level of loss and noise. The idea of utilizing quantum entanglement was not new at the time; quantum entanglement has captured physicists' and engineers' attention for many years. Entangled photons possess greater correlation between the pair than classical physics allows, and that is essential for applications such as quantum cryptography [2], quantum computing [3], and quantum metrology [4]. Unfortunately, quantum entanglement is fragile; it is susceptible to degradation due to noise and loss. Applications of quantum entanglement are often carried out in a well-controlled environment, where noise, absorption, air turbulence, and such are minimal. In contrast, Lloyd's proposal is remarkable because it enables us to apply quantum entanglement even in a noisy and lossy environment.

The concept of quantum illumination has been studied by several groups since Lloyd's proposal. In 2008, Tan *et al.* published a paper which works out a full Gaussian state treatment of quantum illumination [5]. In a paper published in 2009, Shapiro and Lloyd prove that the single-photon quantum illumination scheme can outperform a coherent-state classical source of the same average photon number [6]. In the same year, Shapiro published a paper on how to defeat passive eavesdropping in direct communication with quantum illumination [7]. Experimental demonstrations were made in 2013. In early 2013, Lopaeva *et al.* demonstrated a target detection

scheme using quantum illumination [8]. Later that year, Zhang *et al.* of our group demonstrated an entanglement-based secure communication using quantum illumination [9].

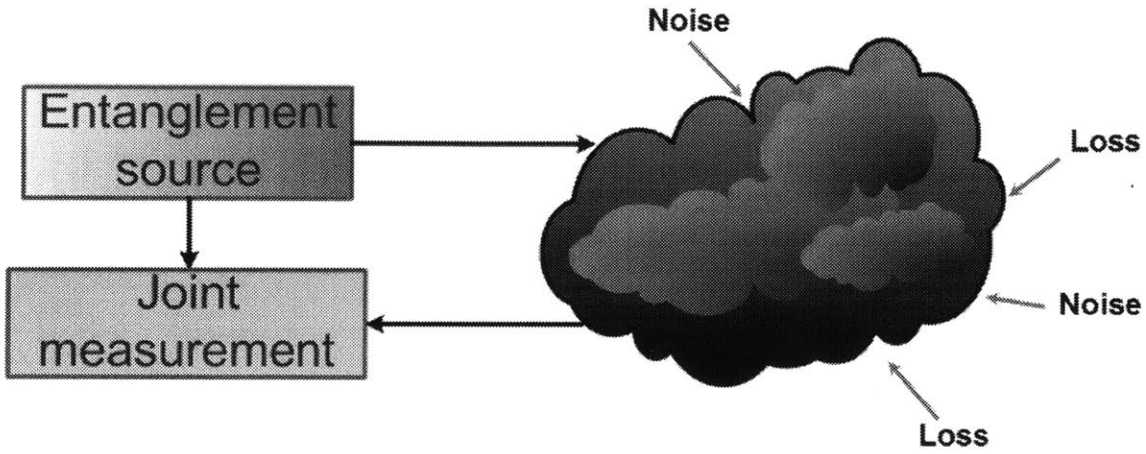

Figure 1-1: Basic schematic of quantum illumination.

The basic principle of quantum illumination is rather simple as shown in Fig. 1-1. Entangled light, consisting of multimode signal and idler beams, are prepared using spontaneous parametric downconversion (SPDC) in a nonlinear crystal. In the case of target detection, the signal beam is transmitted to the target of interest, whereas the idler beam is retained for joint measurement. If the target is present, the signal light is reflected and the detector performs a joint measurement with the retained idler light. In the case of secure communication, the signal light is transmitted from Alice to Bob, and the idler light is retained by Alice. The signal is message-encoded by Bob who masks the message with noise before being sent back to Alice. Alice then decodes the message by a joint measurement between the received signal and the retained idler. For both cases, the experiments are done in an environment with a large amount of noise and loss, such that the signal and idler beams are no longer quantum entangled at the joint measurement apparatus. However, target detection and secure communication using quantum illumination still provide improvements over classical inputs because the previously-entangled light yields a correlation that cannot be achieved with classical input light for the given loss and noise.

Zhang *et al.* demonstrated secure communication in a fiber channel [9]. This thesis extends Zhang *et al.*'s work to a free-space channel. Unlike a fiber channel, a free-space channel is susceptible to performance degradation due to air turbulence. Because a single spatial mode of light is essential in the QI protocol, if the beam path is affected by air turbulence, the power and phase can fluctuate., which in turn can affect the interferometric measurement performance. In order to fix this issue, we need a servo system that can stabilize the beam path. The servo system utilizes the X and Y tilts of a single piezoelectrically driven mirror mount, together with a quadrant detector, to stabilize the beam location at the collimation optics of the free-space path. To demonstrate the QI-based secure communication with a free-space propagation channel, we have implemented a heat source to simulate air turbulence and measured the experimental performance. This demonstration is an important first step toward QI-based quantum communication in free space, such as satellite communication or naval communication.

Chapter 2

Secure Communication Protocol

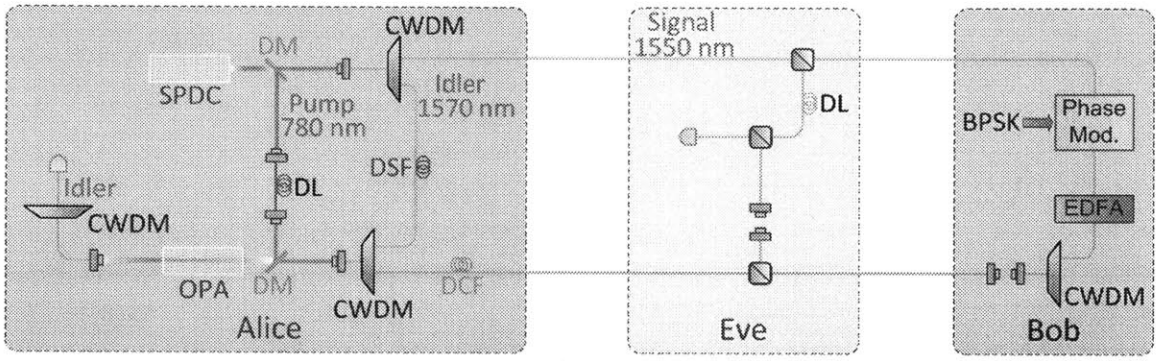

Figure 2-1: Experimental setup with fiber channels. SPDC: spontaneous parametric downconverter; DM: dichroic mirror; C: fiber collimator; CWDM: coarse wavelength-division multiplexer; BS: beam splitter; Attn: attenuator; EDFA: erbium-doped fiber amplifier; DL: delay line; PC: polarization convtoller; PM: phase modulator; AAG: adjustable air gap; Pol: polarizer; DCF: dispersion-compensating fiber; DSF: dispersion-shifted fiber; TEC: thermo-electric cooler; OPA: optical parametric amplifier; D: photodetector. Figure reproduced from Ref. [9].

This chapter discusses how the QI-based secure communication protocol is designed and analyzes the theoretical model, as shown schematically in Fig. 2-1 and Fig. 2-2, respectively. Note that the models and derivations used in this chapter are based on Ref. [9] and its supplemental material. Alice prepares the entangled beam and sends the signal light to Bob. Bob encodes the message using binary phase-shift keying, injects noise to the encoded signal beam, and sends it back to Alice. Eavesdropper Eve tries to tap the Alice-to-Bob and Bob-to-Alice channels, which will be

discussed later in this chapter.

The single-mode signal and idler annihilation operators are denoted by $\{\hat{a}_{S_i}\}$ and $\{\hat{a}_{I_i}\}$, respectively for Alice's spontaneous parametric downconverter (SPDC). The losses in Alice, Bob, and Eve's terminals and the propagation channels are denoted by the transmissivities κ_I, κ_A, κ_1, κ_B, κ'_B, κ_2, κ'_A, κ_d, κ_E, and κ'_d. The corresponding vacuum-state auxiliary modes are represented by $\{\hat{v}_I$, $\hat{v}_A$, $\hat{v}_1$, $\hat{v}_B$, $\hat{v}'_B$, $\hat{v}_2$, $\hat{v}'_A$, $\hat{v}_d$, $\hat{v}_E$, $\hat{v}'_d\}$. Bob's binary phase-shift keying (BPSK) modulates the signal by either 0 or π radian, which are represented by the superscripts $\pm$. Note that the modes Alice and Eve measure are denoted by $\hat{a}_I^{\pm}$ and $\hat{a}_E^{\pm}$, respectively. G_A and G_B represent Alice's optical parametric amplifier (OPA) gain and Bob's erbium-doped fiber amplifier (EDFA) gain, respectively.

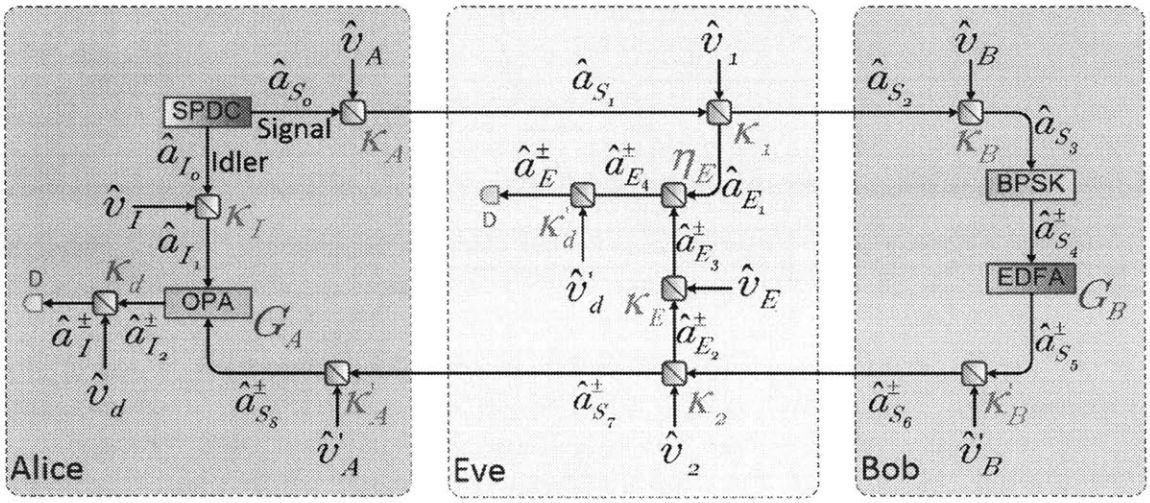

Figure 2-2: Theoretical model for tQI-based secure communication. BPSK: binary phase-shift keying. Figure reproduced from Ref. [9].

2.1 Entanglement generation

Alice prepares maximally entangled signal and idler photons, using a spontaneous parametric downconverter (SPDC), a 20 mm type-0 phase-matched MgO-doped periodically poled lithium niobate (MgO:PPLN) crystal, in which the pump, signal, and idler photons are all polarized along the crystal's z axis. The crystal is continuous-

wave (cw) pumped at 780 nm:

$$\lambda_P = 780 \text{ nm}. \tag{2.1}$$

The generated signal and idler photons have wavelengths at 1550 nm and 1570 nm:

$$\lambda_S = 1550 \text{ nm} \tag{2.2}$$

$$\lambda_I = 1570 \text{ nm}. \tag{2.3}$$

The signal and idler pairs are generated at the same time and dictated by conservation of energy: $\hbar\omega_P = \hbar\omega_S + \hbar\omega_I$. Hence, the pairs are time-and-energy entangled. The phase mismatch condition between the pump, signal, idler photons, and the crystal lattice is given by

$$\Delta k_z = \left| \vec{k}_P - \vec{k}_S - \vec{k}_I - \vec{k}_{pp} \right|, \tag{2.4}$$

where $\vec{k}_{pp}$ is the momentum transferred to the output photons from the crystal. Note that the refractive index of crystal is dependent on the input wavelength and temperature. When the phase is exactly matched ($\Delta k_z = 0$), there is a maximum power transfer.

In terms of the theoretical model, the Alice's SPDC produces the signal-idler mode pairs, which the signal and idler annihilation operators $\{\hat{a}_{S_i}\}$ and $\{\hat{a_{I_i}}\}$ act on.

When the pump power is about 136 mW, the SPDC generates on average a source brightness of $N_S = 0.001$ signal and idler photons per mode. The bandwidth of the generated signal and idler photons is 2 THz, and there are 4×10^6 mode pairs per data bit. After the signal and idler pairs are generated, a dichroic mirror separates the pairs from the pump beam at 780 nm and coupled to a single-mode fiber. A coarse wavelength-division multiplexer (CWDM) seperates the signal beam from the idler

beam. The pump and idler beams are retained for joint measurement. For the idler beam, Alice uses a dispersion-shifted fiber (Corning LEAF fiber), whose length is chosen to match the Alic-to-Bob-to-Alice propagation delay seen by the signal beam.

2.2 Message Encoding

The signal beam is transmitted to Bob through a single-mode fiber (SMF). After he makes a polarization correction, he encodes his message by binary phase-shift keying (BPSK). He encodes his message bits at a rate of 500 kbits/s; the per-bit duration T is 2 μs. The message bit 0 corresponds to 0 radian shift in phase, whereas the message bit 1 corresponds to π radian shift in phase. Per information bit, there are $M = TW \approx 4 \times 10^6$ signal-idler mode pairs, where W $\approx$ 2 THz is the band limit imposed by the 16-nm bandwidth of the CWDM. Each of the signal-idler mode pairs are independent and identically distributed. In this experiment, BPSK is driven by a pseudorandom bit sequence from a bit-error rate (BER) tester.

In terms of the theoretical model, $\{\hat{a}_{S_2}\}$ is the annihilation operators for the signal light that reaches Bob. Then, propagation and detection loss are accounted for $\{\hat{a}_{S_2}\}$, and we get the following:

$$\hat{a}_{S_3} = \sqrt{\kappa_B}\,\hat{a}_{S_2} + \sqrt{1-\kappa_B}\,\hat{v}_B, \tag{2.5}$$

where κ_B and $\hat{v_B}$ are the transmissivity and vacuum-state auxiliary mode for Bob's terminal. For each signal mode, the BPSK modulator is modeled by the following annihilation-operator relation:

$$\hat{a}^{\pm}_{S_4} = \pm\hat{a}_{S_4} \tag{2.6}$$

where $\pm$ represents the phase-shift (and the common bit value) applied to all M signal modes.

2.3 Noise Injection

After the BPSK stage, Bob sends the signal light through an EDFA, whose measured gain is approximately 1.34×10^4. The EDFA is used to boost the signal amplitude and to inject noise to mask the message. Bob's EDFA is modeled by the following annihilation-operator relation:

$$\hat{a}^{\pm}_{S_5} = \sqrt{G_B}\,\hat{a}^{\pm}_{S_4} + \sqrt{G_B - 1}\,\hat{a}^{\dagger}_{SE} \tag{2.7}$$

where $\hat{a}^{\dagger}_{SE}$ is a thermal-state spontaneous-emission mode. Its amplified spontaneous emission (ASE) noise at the amplifier's output has per-mode average photon number $N_B \approx 1.46 \times 10^4$, which is calculated from the following equation:

$$N_B = (G_B - 1)(< \hat{a}^{\dagger}_{SE}\hat{a}_{SE} > +1). \tag{2.8}$$

2.4 Joint Measurement

After the EDFA stage, Bob sends the signal beam back to Alice through a single-mode fiber. Then, she decodes the message bits by a joint measurement between the returned signal beam and the retained idler beam using a low-gain optical parametric amplifier (OPA) followed by direct detection. The signal and idler are combined using a CWDM, and they are combined with the pump beam using a free-space dichroic mirror. Alice couples the combined beams into a 20 mm MgO:PPLN crystal that serves as the OPA. At the OPA, the cross correlation between the phase-modulated signal and the idler is converted to amplitude modulation in the output idler. After filtering out the output idler from the rest of the beam, the message bits are directly detected by a photodiode, and we determine their bit values of 0 or 1 based on threshold-decision logic implemented in the BER tester. Zhang *et al.* used an avalanche photodiode (APD) with 45% efficiency which includes coupling and filter

insertion loss.

2.5 Eavesdropping

One possible scheme for (passive) eavesdropping is to tap the Alice-to-Bob and Bob-to-Alice channels and perform a joint classical-state measurement. In this measurement, Eve taps 50% of light in the Alice-to-Bob channel and taps 10% from the Bob-to-Alice channel. As a consequence, Alice and Bob suffer approximately 16.4 dB loss from the Alice-to-Bob channel and approximately 4.1 dB loss from the Bob-to-Alice channel, both including SMF coupling loss, fiber-optic component insertion loss, and Eve's tapping. Because Eve can only perform classical joint measurement, Alice's cross-correlation signature between the returned signal and retained idler is much stronger than Eve's.

2.6 Result of the Fiber Channel Communication

Table 2.1 lists the experimentally-determined parameter values for obtaining the bit-error-rate (BER) data with the fiber channel. The symbols in the table correspond to those in Fig. 2-2.

From a basic communication model of quantum illumination, one derives the mode-pair photon statistics. The detailed derivation can be found from [9] and its supplemental material. Alice's continuous-wave spontaneous parametric downconverter initially generates a single signal-idler mode pair $\{\hat{a}_{S_0}, \hat{a}_{I_0}\}$ in the maximally-entangled, zero-mean, jointly-Gaussian state $\hat{\rho}_{SI}$. We can compute its density operator by computing the covariance matrix Γ_{SI}:

Parameter	Symbol	Value
Alice's fluorescence bandwidth	W	2 THz
Alice's signal transmissivity	κ_A	0.74
Alice-to-Bob transmissivity	κ_1	0.50
Bob's pre-EDFA transmissivity	κ_B	0.43
Bob's BPSK modulation rate	R	500 kbit/s
Bob's BPSK bit duration	T	2 μ s
Bob's EDFA gain	G_B	1.34×10^4
Bob's EDFA per-mode ASE	N_B	1.46×10^4
Bob's post-EDFA transmissivity	κ'_B	0.39
Bob-to-Alice transmissivity	κ_2	0.90
Alice's return transmissivity	κ'_A	0.41
Alice's idler transmissivity	κ_I	0.39
Alice's OPA gain - 1	G_A - 1	1.86×10^{-5}
Alice's detection efficiency	κ_d	0.45
Alice's modulation-depth efficiency	η_d^A	0.52
Alice's number of mode pairs	M	4×10^6
Eve's return transmissivity	κ_E	0.013
Eve's mixing ransmissivity	η_E	0.99
Eve's detection efficiency	κ'_d	0.5
Eve's modulation-depth efficiency	η_d^E	0.17
APD noise figure	F_{APD}	3.0
Electronics-noise variance	σ_D^2	6.0×10^{-3}

Table 2.1: Experimentally-determined parameter values for the fiber communication channels [9].

$$\Gamma_{SI} = \langle [\hat{a}^\dagger_{S_0} \hat{a}^\dagger_{I_0} \hat{a}_{S_0} \hat{a}_{S_0}]^T [\hat{a}_{S_0} \hat{a}_{I_0} \hat{a}^\dagger_{S_0} \hat{a}^\dagger_{S_0}] \rangle \tag{2.9}$$

$$= \begin{bmatrix} N_S & 0 & 0 & \sqrt{N_S(N_S+1)} \\ 0 & N_S & \sqrt{N_S(N_S+1)} & 0 \\ 0 & \sqrt{N_S(N_S+1)} & N_S & 0 \\ \sqrt{N_S(N_S+1)} & 0 & 0 & N_S \end{bmatrix} \tag{2.10}$$

Note that N_S is the source brightness, average number of signal-idler photon pairs per mode. With this density operator, the input-output operator evolutions associated with the beam splitters, BPSK, and EPFA models, we can determine Alice and Eve's single-mode photon-counting statistics. The statistics are Bose-Einstein with variances that satisfy

$$\sigma^2_{A_\pm} = \langle \hat{a}^{\pm\dagger}_I \hat{a}^\pm_I \rangle (\langle \hat{a}^{\pm\dagger}_I \hat{a}^\pm_I \rangle + 1) \tag{2.11}$$

$$= N^\pm_A (N^\pm_A + 1), \tag{2.12}$$

and

$$\sigma^2_{E_\pm} = \langle \hat{a}^{\pm\dagger}_E \hat{a}^\pm_E \rangle (\langle \hat{a}^{\pm\dagger}_E \hat{a}^\pm_E \rangle + 1) \tag{2.13}$$

$$= N^\pm_E (N^\pm_E + 1), \tag{2.14}$$

where $N^\pm_A$ and $N^\pm_E$ are Alice and Eve's average photon numbers, respectively. Their average photon numbers can be found, while considering the effect of imperfect dispersion compensation and sub-optimal mode-pair coupling. For Alice we have

$$N_A^{\pm} = \kappa_d \langle \hat{a}_I^{\pm\dagger} \hat{a}_I^{\pm} \rangle \tag{2.15}$$

$$= \kappa_d G_A \langle \hat{a}_{I_1}^{\dagger} \hat{a}_{I_1} \rangle + \kappa_d (G_A - 1) + \kappa_d (G_A - 1) \langle \hat{a}_{S_8}^{\pm\dagger} \hat{a}_{S_8}^{\pm} \rangle$$
$$\pm 2\eta_d^A \kappa_d \sqrt{G_A(G_A - 1)}\, \mathrm{Re}(\langle \hat{a}_{I_1} \hat{a}_{S_8}^{\pm} \rangle), \tag{2.16}$$

where

$$\langle \hat{a}_{I_1}^{\dagger} \hat{a}_{I_1} \rangle = \kappa_I N_S, \tag{2.17}$$

$$\langle \hat{a}_{S_8}^{\pm\dagger} \hat{a}_{S_8}^{\pm} \rangle = \kappa'_A \kappa_2 \kappa'_B G_B \kappa_B \kappa_1 \kappa_A N_S + \kappa'_A \kappa_2 \kappa'_B N_B, \tag{2.18}$$

and

$$\langle \hat{a}_{I_1} \hat{a}_{S_8}^{\pm} \rangle = \pm \sqrt{\kappa_I \kappa'_A \kappa_2 \kappa'_B G_B \kappa_B \kappa_1 \kappa_A N_S (N_S + 1)}. \tag{2.19}$$

Combining the above results we obtain,

$$N_A^{\pm} = \kappa_d G_A \kappa_I N_S + \kappa_d (G_A - 1) + \kappa_d (G_A - 1)(\kappa'_A \kappa_2 \kappa'_B G_B \kappa_B \kappa_1 \kappa_A N_S + \kappa'_A \kappa_2 \kappa'_B N_B)$$
$$\pm 2\eta_d^A \kappa_d \sqrt{G_A(G_A - 1)\kappa_I \kappa'_A \kappa_2 \kappa'_B G_B \kappa_B \kappa_1 \kappa_A N_S (N_S + 1)}. \tag{2.20}$$

Similary for Eve, we obtain

$$N_E^{\pm} = \kappa'_d \eta_E (1 - \kappa_1) \kappa_A N_S + \kappa'_d (1 - \eta_E) \kappa_E (1 - \kappa_2) \kappa'_B G_B \kappa_B \kappa_1 \kappa_A N_S$$
$$+ \kappa'_d (1 - \eta_E) \kappa_E (1 - \kappa_2) \kappa'_B N_B$$
$$\pm 2\eta_d^E \kappa'_d \sqrt{\eta_E (1 - \eta_E)(1 - \kappa_1) \kappa_A^2 \kappa_E (1 - \kappa_2) \kappa'_B G_B \kappa_B \kappa_1 N_S^2}. \tag{2.21}$$

From above, we have derived the per-mode conditional variance for Alice and Eve's

ideal receivers, $\sigma^2_{A\pm}$ and $\sigma^2_{E\pm}$, when Bob's BPSK modulation is 0 radian or π radian. However, we also have to consider Alice and Eve's avalanche photodiodes' noise figure F_{APD} and electronic-noise variance σ^2_D of their detection systems. Moreover, Alice's OPA receiver has a per-mode conditional variance $\sigma^2_{P\pm} = 0.2\sigma^2_{A\pm}$, which comes from pump-power fluctuations. With these conditions, we can find their total per-mode conditional variances

$$(\sigma^{\text{tot}}_{A\pm})^2 = \text{F}_{APD}\ (\sigma^2_{A\pm} + \sigma^2_{P\pm}) + \sigma^2_D \tag{2.22}$$

and

$$(\sigma^{\text{tot}}_{E\pm})^2 = \text{F}_{APD}\ \sigma^2_{E\pm} + \sigma^2_D. \tag{2.23}$$

The experimentally-determined parameter values are listed in table 2.1. With these values, we can find Alice and Eve's BER:

$$\text{BER}_A = \text{Q}\Big(\frac{\sqrt{M}\zeta_A\sqrt{N_S(N_S+1)}}{\sigma^{\text{tot}}_{A+} + \sigma^{\text{tot}}_{A-}}\Big), \tag{2.24}$$

$$\text{BER}_E = \text{Q}\Big(\frac{\sqrt{M}\zeta_E N_S}{\sigma^{\text{tot}}_{E+} + \sigma^{\text{tot}}_{E-}}\Big). \tag{2.25}$$

Note that Q refers to the tail integral of the standard Gaussian probability density, and ζ_A and ζ_E refer to the transmission efficiencies for Alice and Eve, respectively. For calculating the transmission efficiencies, we have used

$$\zeta_A\sqrt{N_S(N_S+1)} = N^+_A - N^-_A, \tag{2.26}$$

$$\zeta_E N_S = N^+_E - N^-_E. \tag{2.27}$$

Fig. 2-3 is a collection of BER_A and BER_E of various cases, as described in its caption. The dotted blue line is the theoretically predicted BER_A when Alice uses a maximally entangled photon source and an ideal OPA receiver. The ideal case as-

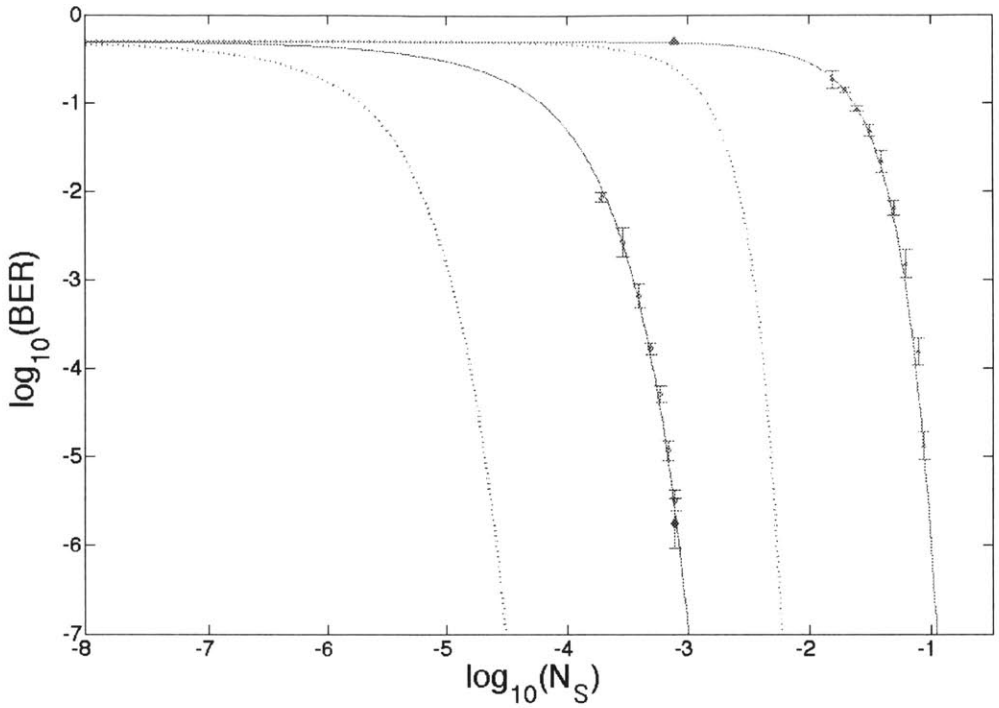

Figure 2-3: Plots of BER_A and BER_E as functions of source brightness N_S for 500 kbit/s communication. Blue-dotted line: BER_A for ideal OPA receiver; Blue solid line: BER_A for actual OPA receiver; Green-dotted line: BER_E for ideal receiver; Green solid line: BER_E for actual receiver. Error bars represent the experimental data collected with the parameter values in table 2.1. [9]

sumes that there is no loss of modulation depth due to residual dispersion or suboptimal mode-pair coupling, unity detection efficiency, unity APD noise figure, no OPA pump-power fluctuations, and no electronics noise, whereas the actual case with the experimentally determined parameter values (table 2.1) is drawn with the solid blue line. The dotted green line is the theoretically predicted BER_E when Eve employs an ideal interference receiver. For Eve, it does not matter whether Alice generated her photons with a maximally entangled SPDC source or a maximally correlated classical source. The solid green line is for the actual case where the parameters are listed in the same table. Note that if Alice uses a maximally correlated classical source to generate the photon pairs, her BER_A measured with an ideal receiver would be the same as BER_E for the ideal case.

We can observe from Fig. 2-3 that the experimental results are in excellent agree-

ment with theory. Moreover, using quantum illumination, Alice's performance far exceeds that of Eve for $N_S \ll 1$. For example, when $N_S = 7.81 \times 10^{-4}$ with Alice's OPA gain $G_A - 1 = 2.48 \times 10^{-5}$, we obtain $BER_A = 1.78 \times 10^{-6}$, but $BER_E \approx 50\%$. In Fig. 2-4, 25 bits of OPA receiver output of Alice (blue) and Bob's corresponding modulation waveform (red) are shown with the electronic signal from OPA being AC-coupled. We can easily observe that Alice's received message can be easily decoded with high signal-to-noise ratio.

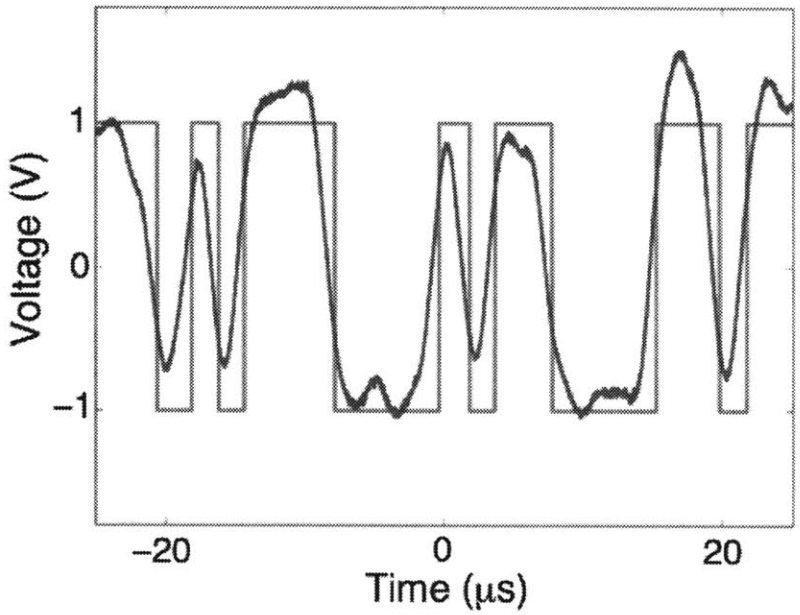

Figure 2-4: Trace of 25 bits of OPA receiver output (blue) and Bob's corresponding modulation waveform (red). [9]

A large performance gap between an entangled-state input and a classical-state input in a lossy and noisy channel is possible even though the joint state of Alice's returned and retained photons is classical. According to [9], we can achieve such a condition by having

$$N_B \geq N_B^{\text{threshold}} = \kappa_A \kappa_1 \kappa_B G_B. \tag{2.28}$$

For this case, we have that $N_B^{\text{threshold}} = 2.14 \times 10^3$ and $N_B = 1.46 \times 10^4$, which exceeds $N_B^{\text{threshold}}$ by 8.3 dB. This ensures that, by having entanglement, Alice can obtain immunity to Eve's passive eavesdropping.

Chapter 3

QI-based Secure Communication with a Free-space Link

The first demonstration of secure communication using quantum illumination was done completely through the optical fiber channels [9]. Although Zheshen *et al.* implemented a small free-space gap that is about 10 cm in length located after the EDFA as shown in Fig. 2-1, the gap was in Bob's side. Quantum illumination is a protocol that requires an interferometric measurement. Hence, the path lengths for signal and idler have to be matched precisely. The small free-space gap is only used for the fine path length adjustment for the signal beam. Other than that, the Alice-to-Bob and Bob-to-Alice channels use only optical fibers.

In this chapter, we discuss how to replace the communication channel between Alice and Bob with a free-space channel. Free-space communication is essential when optical fibers are physically impossible to connect between two parties. Satellite communication and naval communication are typical scenarios where we need to use free-space channels. Unfortunately, there are many factors that need to be considered for free-space communication. Unlike an optical fiber which guides the beam within a confined mode, a free-space channel can be significantly affected by environment. For example, in the case of naval communication, an ocean can be heated by the sun and produces temperature gradients along the beam path. Water vapor and wind can affect the beam path as well. In addition, the ship's movement must be

precisely tracked to maintain the communication link. All of these can significantly affect the communication performance because the QI protocol uses a single spatial mode for transmission and reception. Moreover, as the beam passes through a turbulent environment, the path length can fluctuate and must be stabilized for the QI interferometric measurements.

In the following sections, we will discuss steps takes to implement a free-space channel for QI secure communication. We have designed a servo system to stablize the free-space communication between Alice and Bob. The servo system consists of multiple components; each will be closely analyzed. We have implemented a heating plate to simulate a free-space turbulent link. This heating plate will be used to test how good the servo system is.

3.1 Free-space Channel Communication via Quantum Illumination

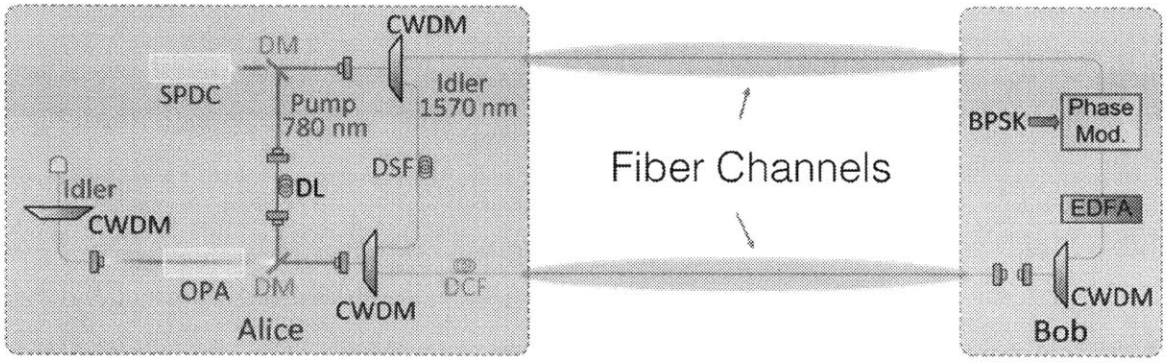

Figure 3-1: Fiber channels between Alice and Bob.

In the fiber-channel implementation of QI-based secur communication, there are two optical fibers connecting between Alice and Bob, as shown in Fig. 3-1. One is from Alice to Bob, and the other from Bob to Alice. We replace each of these fiber channels separately and examine how air fluctuation affects the communication in each case.

Fig. 3-2 is the proposed method for correcting the beam angle for the Alice-to-Bob

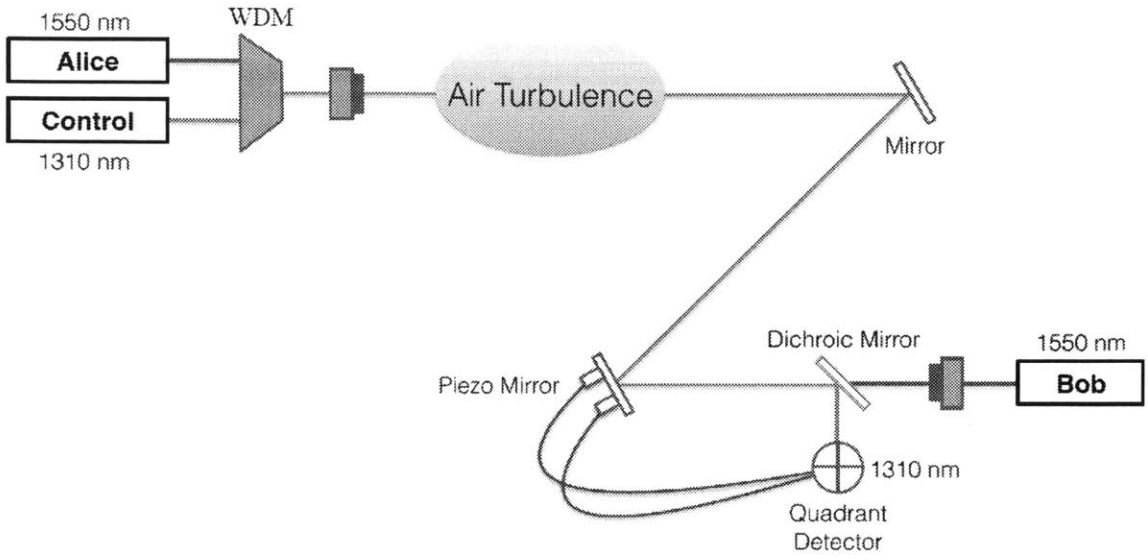

Figure 3-2: Servo system design for the Alice-to-Bob free-space channel. For the experiment, we have set the following distances: 15 cm from Alice's collimator to air-turbulence zone; 80 cm from the piezo mirror to Bob's collimator; the total distance between Alice's and Bob's collimators is 1.2 m. Note that the figure is not drawn to scale.

channel. For this channel, the servo system is placed at Bob's side. For controlling the servo loop system, we use a wavelength-division multiplexer (WDM) to combine a signal beam at 1550 nm and a control beam at 1310 nm at Alice. We cannot use the signal beam for servo control because its power is too low for the servo quadrant detector.

Alice sends the combined beam through an area of air turbulence which is generated by a heating plate. When the beam path is affected by air fluctuation, the direction of propagation tilts by some small angle, and a small deviation in angle can significantly affect the coupling into the fiber. Once the combined light reaches Bob, a dichroic mirror separates the two beams. The dichroic mirror reflects the control light of 1310 nm to the position sensing photodetector, whereas the signal light passes through and goes into the fiber coupler.

We use a quadrant detector as the position sensing detector. The quadrant detector locates the position of the beam and sends the positional error signals to the

piezoelectric adjusters that are attached to the kinematic mirror mount. We use two of the three piezoelectric adjusters of the mirror mount to change the angle of the reflected beam along the horizontal and vertical directions. Based on the signals coming from the quadrant detector to the signal filter, the mirror tilts and corrects the angle of the beam to stabilize the coupled power. More detailed analysis on each component comes later in this chapter.

3.2 Fiber Coupling

Fiber coupling is not a simple task. In order to optimally couple light into the fiber, the light and the fiber must be mode-matched. Therefore, in principle, we need to have at least four degrees of freedom, assuming that the size of the beam matches to that of fiber. For this particular design, the air fluctuation generated by the heat plate will displace the beam from the optimal position. However, we assume that the effect is not too severe, such that it does not move the beam too far from the optimal position. Both the angle and the position of the beam will be shifted by the turbulence, but the fiber collimator has a large enough acceptance angle that we can stabilize the coupled power by simply correcting the tilting angles of the piezo mirror. In the experimental setup, the free-space communication distance between Alice and Bob is approximately 120 cm.

When we implement the Bob-to-Alice free-space channel, the heat plate is located 15 cm from Bob, and the piezoelectric mirror mount is located 80 cm from Alice. A WDM combines the control beam (1310 nm) and the signal beam (1550 nm) on Bob's side. According to the specification sheet, the WDM has 0.22 dB and 0.11 dB insertion loss at 1310 nm and 1550 nm, respectively. For both Alice and Bob, we use Thorlabs F230FC collimators. Each collimator is anti-reflection coated for 1550 nm and has a focal length of 4.67 mm with a numerical apperture (NA) of 0.53. For both sides, we use uncoated lenses of 15 cm focal length to collimate the beam. For this experiment, the beam size is about a few hundred μm, but the beam size should be much larger for greater propagation distances. With no turbulence, the fiber coupling

efficiency is 1.91 mW / 2.13 mW $\approx$ 89% when we use the fiber coated at 1550 nm. The loss mainly comes from the WDM insertion loss and the uncoated lenses.

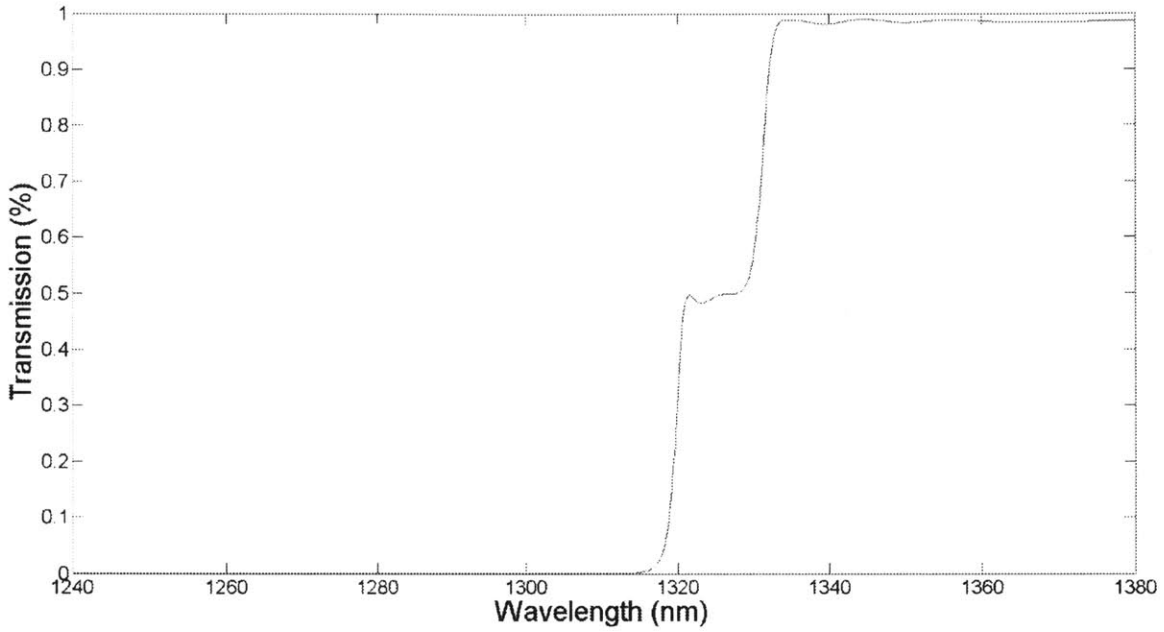

Figure 3-3: Wavelength vs. transmission at 18° angle.

Fig. 3-3 shows the light transmission of the dichroic mirror (PN: BLP01-1319R-25) as a function of wavelength ranged from 1240 nm to 1380 nm at 18° of the incident angle. The data is provided by the manufacturer, Semrock. If the angle of incidence is beyond 20°, too much of 1310 nm light leaks into the fiber coupler, which is undesirable because some unexpected interference can occur. In our setup, the dichroic mirror is at 18°, because of the space needed for component placement. At this angle, it can filter out most of the 1310 nm beam in transmission. We have measured that 0.2 $\mu W/200\ \mu W \approx 0.1\%$ of the 1310 nm light is coupled into the signal fiber.

3.3 Servo Loop Design

Now, let us take a look at the feedback system. As shown in Fig. 3-4, it consists of a quadrant detector, its reader, a mirror mount with piezoelectric adjusters, their voltage drivers, and additional signal-conditioning filters. The following is the description

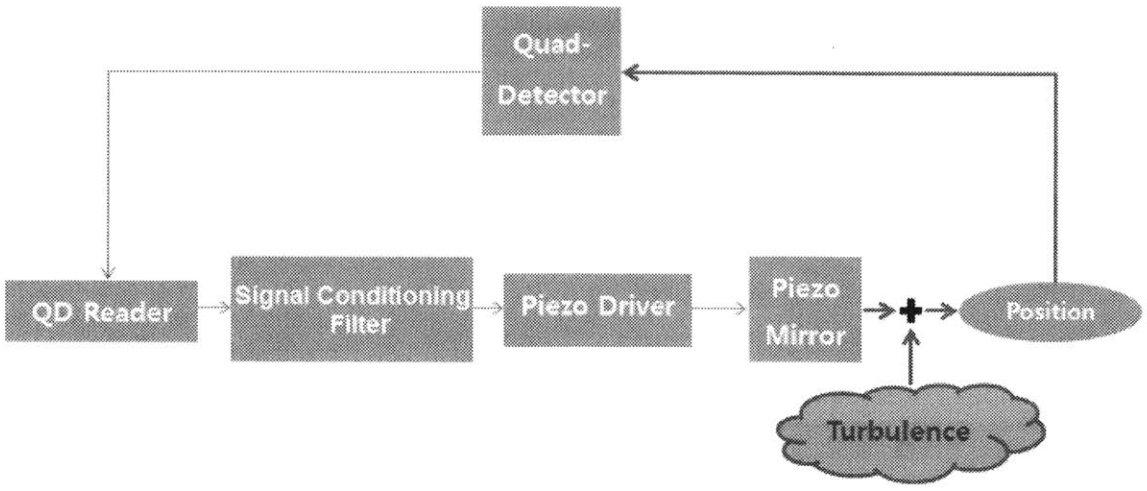

Figure 3-4: Block diagram of the servo loop system; red line symbolizes the light signal, and blue line symbolizes the electric signal; quad-detector: quadrant detector; QD reader: quandrant detector reader.

on how it operates. We first optimize the fiber coupling of the signal light at 1550 nm. The control light at 1310 nm is reflected from the dichoric mirror and aimed at the center of the quadrant detector.

3.3.1 Quadrant Detector and Reader

The quadrant detector is manufactured by Thorlabs. It is made of InGaAs substrate and has the wavelength range of 1000 to 1700 nm. One can monitor the location of the beam on the computer using software provided by Thorlabs. The schematic of the quadrant detector is shown in Fig. 3-5.

The quadrant detector is connected to the quadrant detector reader. The detector is comprised of four photodiodes Q1, Q2, Q3, and Q4. The detector sends the amount of detected light on each photodiode to the reader, and the reader generates positional error signals in the horizontal and vertical directions based on the following equations:

$$\Delta x_{error} = (Q2 + Q3) - (Q1 + Q4), \tag{3.1}$$

$$\Delta y_{error} = (Q1 + Q2) - (Q3 + Q4). \tag{3.2}$$

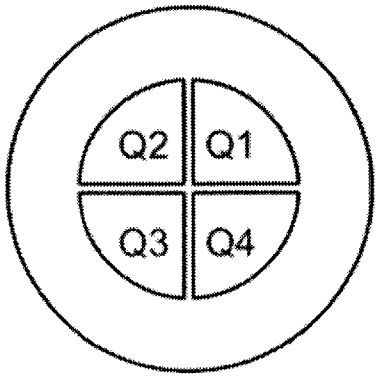

Figure 3-5: Schematic of quadrant detector

Note that Q1, Q2, Q3, and Q4 are the amounts of light on the corresponding photodiodes in terms of voltage. The total amount of light on the detector can be found easily by summing all those values, $SUM = Q1 + Q2 + Q3 + Q4$. Moreover, the actual position of light can be calculated by the following formulas:

$$x = \frac{\Delta L_x}{2} \frac{\Delta x_{error}}{SUM}, \tag{3.3}$$

$$y = \frac{\Delta L_y}{2} \frac{\Delta y_{error}}{SUM}, \tag{3.4}$$

where ΔL_x and ΔL_y are the horizontal and vertical lengths of the detector, respectively. For this component, ΔL_x and ΔL_y are the diameters of the detector, which is 3 mm. Because the size of the detector is only 3 mm, the control beam must be focused and should not exceed 0.5 mm in diameter for the servo system to work properly. If the beam is too large compared to the size of the detector, the reader will not be able to accurately measure the location of the beam and the position sensitivity drops. One should be careful when focusing the beam, because this detector can be damaged by a high incident power of light. The damage threshold is about 100 mW/cm^2.

3.3.2 Piezoelectric Adjusters and Drivers

The signal from the reader is fed to the piezoelectric drivers. The drivers are simple voltage amplifiers which drive the piezoelectric adjusters of the mirror mount. We use two drivers for the horizontal and vertical directions, and the operational voltage range is from 0 to 150 V. The piezoelectric adjusters are located inside the mechanical adjusters of the mirror mount. The mechanical adjusters have the angular range of $\pm 5^{\circ}$, whereas the piezoelectric adjusters have the range of $\pm 500\ \mu rad$.

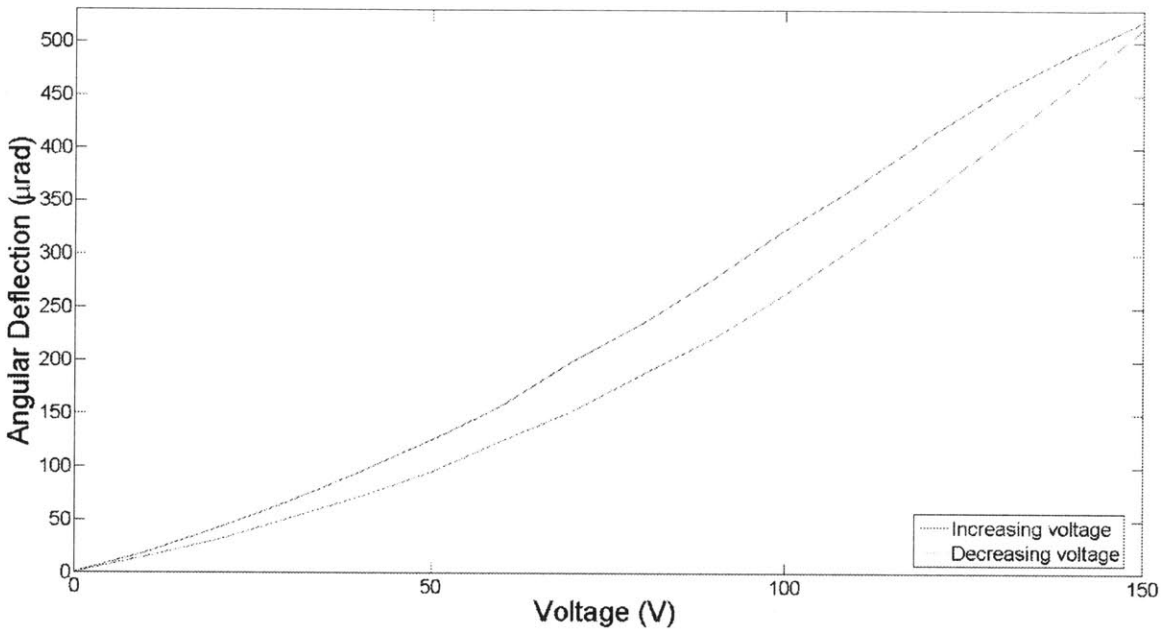

Figure 3-6: Change in angle as a function of the piezo control voltage.

Fig. 3-6 shows the plot of angular deflection as a function of the applied voltage to the piezoelectric adjusters. We can obserse a hysteresis response of the piezoelectric adjuster, which is typical for piezoelectric materials.

3.3.3 Operational Modes

Our system has two operational modes, open-loop and closed-loop modes. When in the open-loop mode, the reader does not generate any error signal. When in the close-loop mode, the error signals are generated and fed into other electronics components, such as piezoelectric drivers. Then, the piezoelectric drivers change the angles of the

mirror mount and modify the location of the beam. From the computer software, one can optimize the closed-loop operation by tuning various parameters. These parameters are feedback gains in the horizontal and vertical directions, proportional gain, and integral gain. The horizontal and vertical feedback gains allow us to control the gain for each direction independently. The proportional gain is the multiplication factor to the error signals, whereas the integral gain is to set how fast the feedback reacts. If the system is not optimized, we can observe some arbitrary oscillations or positive feedback effects, but when it is optimized, we can see that the location of the beam quickly stablizes to the center.

The delay time τ_D that the signal takes to make one round trip of the system is measured to be 200 μs. The unity gain frequency of the whole system f_{unity} is approximately $\frac{1}{11\tau_D} \approx 450$ Hz.

Now, let us analyze the bandwidth of the system. According to the specification sheet, in the open-loop mode, both the detector and the reader have bandwidths of 150 kHz and 100 kHz, respectively. However, for the closed-loop mode, the bandwidth of the reader reduces to 1 kHz. Furthermore, the piezoelectric adjusters have a bandwidth of order of 100 Hz, as measured by the response of tilted angle as a function of input voltages at various frequencies. The overall bandwidth of the system is limited by the piezoelectric adjusters. Hence, this system is not suitable for any operation beyond that range.

3.3.4 Feedback Signal Conditioning

After a few trial-and-errors, we have found that without any additional filters the gain in low frequency range is not enough for our system. Therefore, we have implemented additional filters into the system. Those filters are placed between the quadrant reader and the piezoelectric drivers. One of the additional components we implemented is a 6 dB inverting amplifier. It is applied to both the horizontal and vertical directions and multiplies the input signal by 4.

The other filter is a low-pass step filter which serves as an integrator. The schematic of the filter we use in the setup is shown in Fig. 3-7. This is a simple

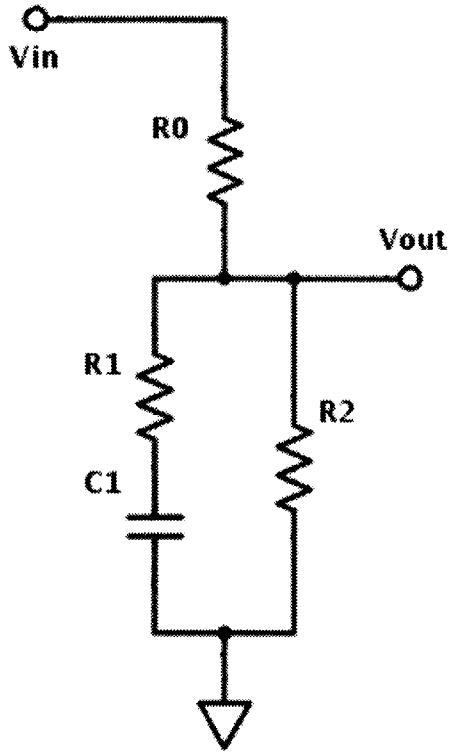

Figure 3-7: Low-pass step filter circuit model.

RC circuit which has two corner frequencies. For the low frequency range, it has 0 dB gain, whereas for the high frequency range, it has a very low gain. The advantage of this circuit is that we set the two corner frequencies independently by choosing appropriate values for resisters and capacitors. Roughly, the lower frequency corner is set by R0 and C1, while the upper frequency corner is determined by R1 and C1. Moreover, the phase shift returns to 0 beyond the second corner frequency. Hence, we do not need to worry about how the filter would affect the total phase of the system at high frequencies. For this experiment, we set the lower corner frequency at 10 Hz, the higher corner frequency at 100 Hz, and the slope to be -6 dB/octave. The bode plots and the corresponding values for electrical components can be found from Fig. 3-8.

3.3.5 Results

Air fluctuation is generated by a heating plate. The device we use is manufactured by Corning and has an adjustable temparature setting. When the heating plate is on, the air above the plate is also heated up. The generated temperature gradient produces air flow in some random manner, and the beam passing through the heating area is affected and changes its direction. We first measured the coupled power without heat and servo. Then, we introduced the heating plate and measured the coupled powers for the open-loop and the closed-loop operations.

Our feedback system is to maximize the fiber coupled power by adjusting the direction of beam propagation from the piezo mirror to the quadrant detector. Typical time traces of the fiber coupled power without and with the feeback are shown in Fig. 3-9. The heating plate is set at level 2.5, which is the hottest temperature that the servo-loop can operate successfully. The traces are measured at the output port of the free-space channel. As shown in Fig. 3-9a, when the servo-loop is inactive, the light coupled to the output collimator frequently fluctuates, and the coupling efficiency can drop by 20% at the maximum. Note that in these plots the optimal coupling is at the photodetector voltage 3.3V. When the servo-loop is on, although there are small fluctuations in the coupling efficiency, the fiber coupling mostly maintains at the optimal level (Fig. 3-9b).

We can also look at the fiber-coupled output spectrally, as shown in Fig. 3-10. The blue line represents the spectrum of coupled power when there is no heat applied. When the heating plate is on (green line), we see that the coupled power fluctuates mostly in the low frequency region. At 3 Hz, the fluctuation increases by 20 dB compared to when there is no heat. The effect of heat becomes insignificant beyond 20 to 25 Hz. Let us take a look at the closed-loop mode. When the feedback system is active, we see that the fluctuation at low frequency is reduced and becomes closer to the curve representing the no-heat no-servo case. At 3 Hz, the servo-loop has reduced the fluctuation by 15 dB. With Fig. 3-9, we conclude that we can significantly improve the fiber coupling in the presence of air fluctuation. This setup is used for the QI-

based secure communication demonstration.

3.4 Path Matching

Because of the addition of the free-space channel, the total distance in the Alice-to-Bob-to-Alice channel has been increased. The free-space channel is measured to be 1.2 m in length. We also have a WDM and an additional single mode fiber that connects from the output of the free-space channel back to the experimental setup. Those lengths are measured to be 3.3 m and 3 m, respectively. For path matching, we have made a LEAF fiber with a length of approximately 7.11 m by fiber splicing technique and implemented on the idler's side. We can finely adjust the length of the signal channel by putting the output coupler of the free-space channel on a translation stage. For this experiment, dispersion effect due to the added fibers is not compensated.

Until now, we only discuss the replacement of the Alice-to-Bob channel. For the Bob-to-Alice channel, it is essentially the same as the Alice-to-Bob channel, except that Alice and Bob are reversed in Fig. 3-2. For this case, the servo loop is placed on Alice's side.

3.5 Part Numbers and Settings

Table 3.1 lists the manufacturers and part numbers for the various components in the servo system. Table 3.2 lists the parameter values for the quadrant detector reader.

Component	Part Number
Quadrant Detector	Thorlabs, PDQ30C
Quadrant Detector Reader	Thorlabs, TPA101
Piezo Driver	Thorlabs, TPZ001
Kinematic Mirror Mount	Thorlabs, Polaris-K1PZ
Inverting Amplifier	SRS, SIM954
Heat Plate	Corning, PC-200
Collimator	Thorlabs, F230FC-1550
Mirrors	Thorlabs, BB05-E04
Dichroic Mirror	Semrock, BLP01-1319R-25

Table 3.1: Table of the manufacturers and part numbers of the system components.

Parameter	Value
Proportional Gain	100
Integral Gain	85
X Feedback Gain	0.9
Y Feedback Gain	0.8

Table 3.2: Table of the parameter values for the quadrant detector reader.

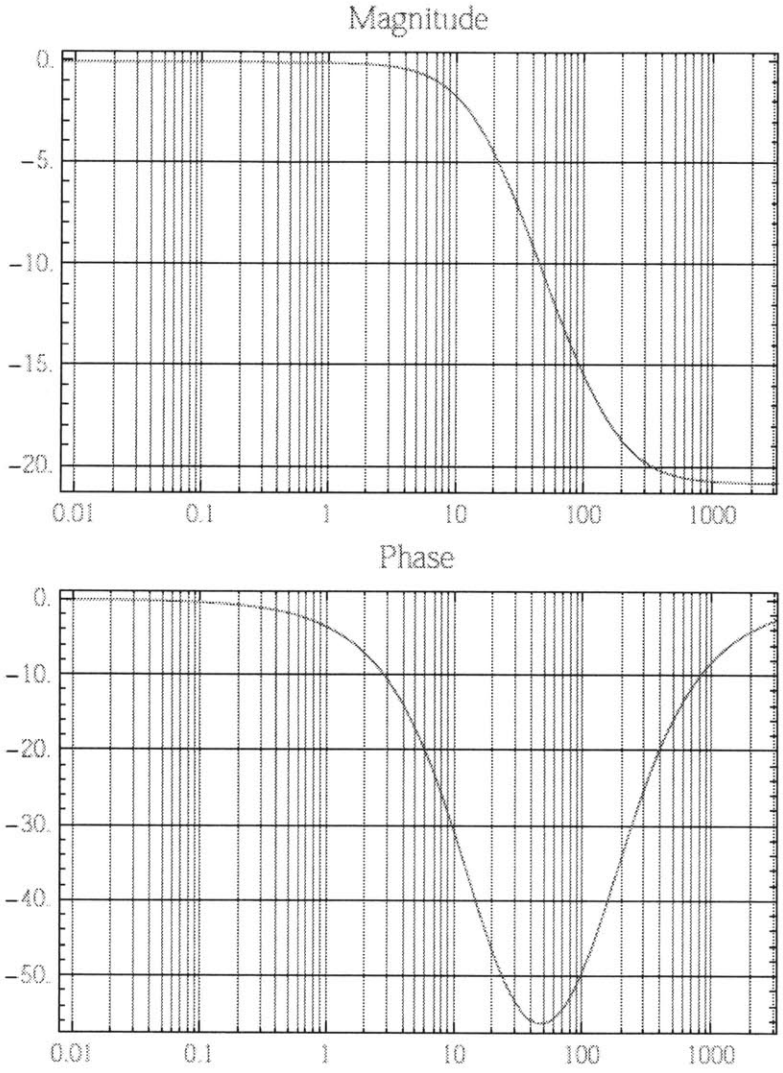

Figure 3-8: Bode plot of low-pass step filter; R0 = 1 kΩ, R1 = 0.1 kΩ, R2 = 100 kΩ, and C1 = 10 μF. Note that the unit is in Hz and dB.

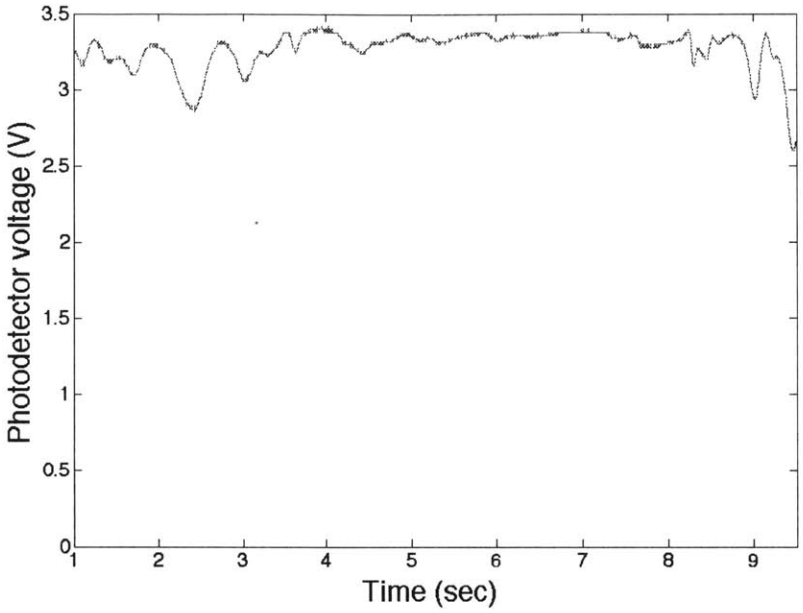

(a) Time trace of the fiber-coupled power for the open-loop mode.

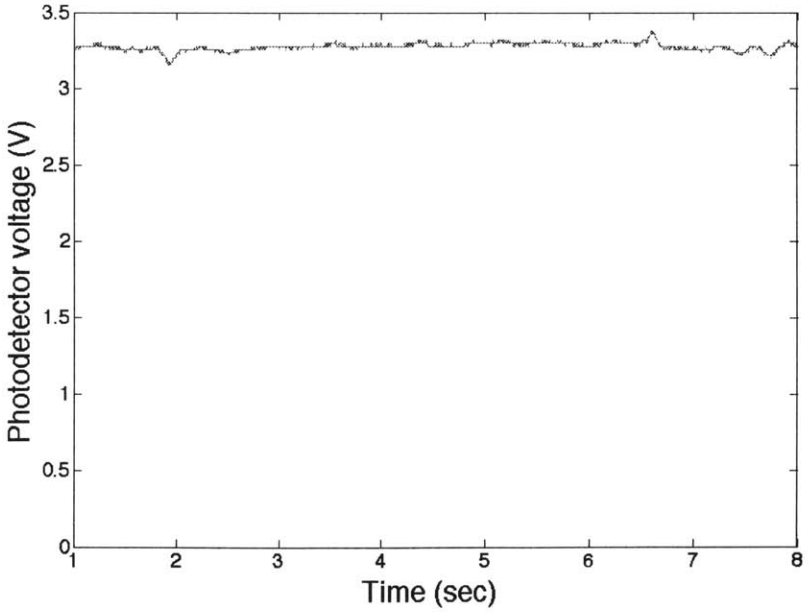

(b) Time trace of the fiber-coupled power for the closed-loop mode.

Figure 3-9: Time trace on the photodetector voltage for the open- and closed-loop modes

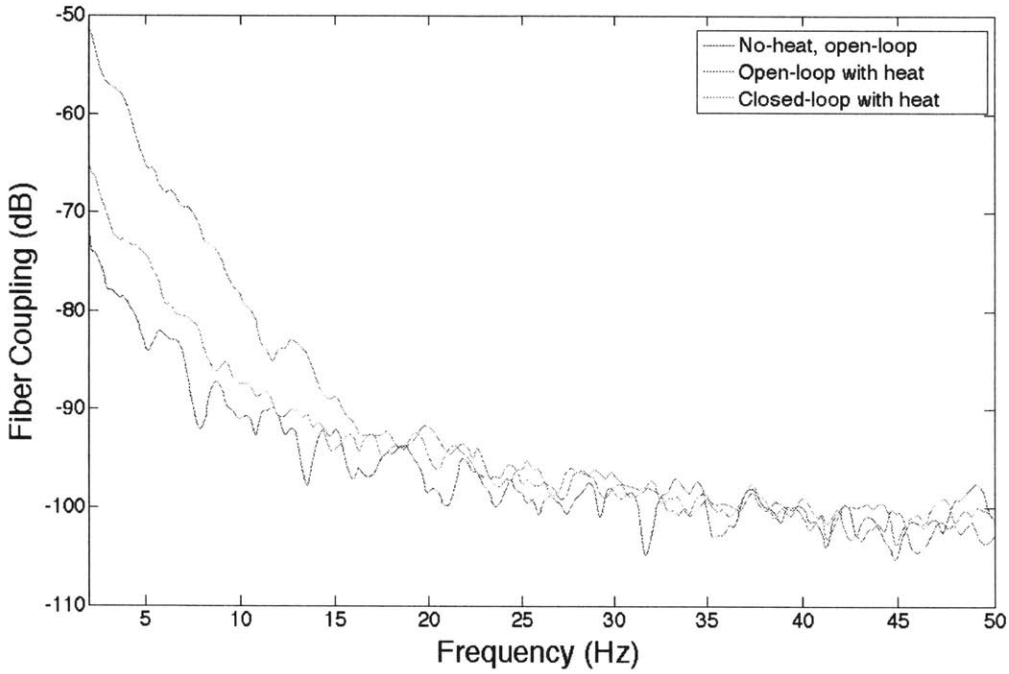

Figure 3-10: Comparison between open-loop and closed-loop responses.

Chapter 4

Experimental Results

For this thesis, we changed several experimental components from the experiment done by Zhang *et al.* [9]. We replaced the APD diode with a PiN diode. Moreover, there are multiple experimental parameter values that we changed for better performance. Those changes are discussed in this chapter. The experiment was done in the following order. We first replaced the fiber channel from Bob to Alice with a free-space channel. We performed a BER measurement with various source brightness N_S values. After that, we turn on a heat source to generate air turbulence. We test and measure the effect of the servo loop that we designed in chapter 3. Then, we do the same measurements for the Alice-to-Bob channel.

4.1 Changes in the Experimental Parameter Values in the Free-space Communication

Compared to the APD detector, a PiN diode has a much lower noise level. For a PiN diode, Alice's total per-mode conditional variance becomes

$$(\sigma_{A\pm}^{\text{tot}})^2 = \sigma_{A\pm}^2 + \sigma_{P\pm}^2 + \sigma_D^2, \tag{4.1}$$

where the electronics-noise variance σ_D^2 is now 0.1, compard with 0.006 for the APD. Fig. 4-1 shows the improved BER_A compared to that measured with an APD detector.

For this measurement, $G_A - 1 = 4.0 \times 10^{-4}$. We observe that the BER_A has improved significantly, at least, by an order of magnitude. For example, when $\mathrm{N}_S = 2.69 \times 10^{-4}$, BER_A has improved from 3.52×10^{-3} to 4.75×10^{-5}, which is 18.7 dB improvement in BER.

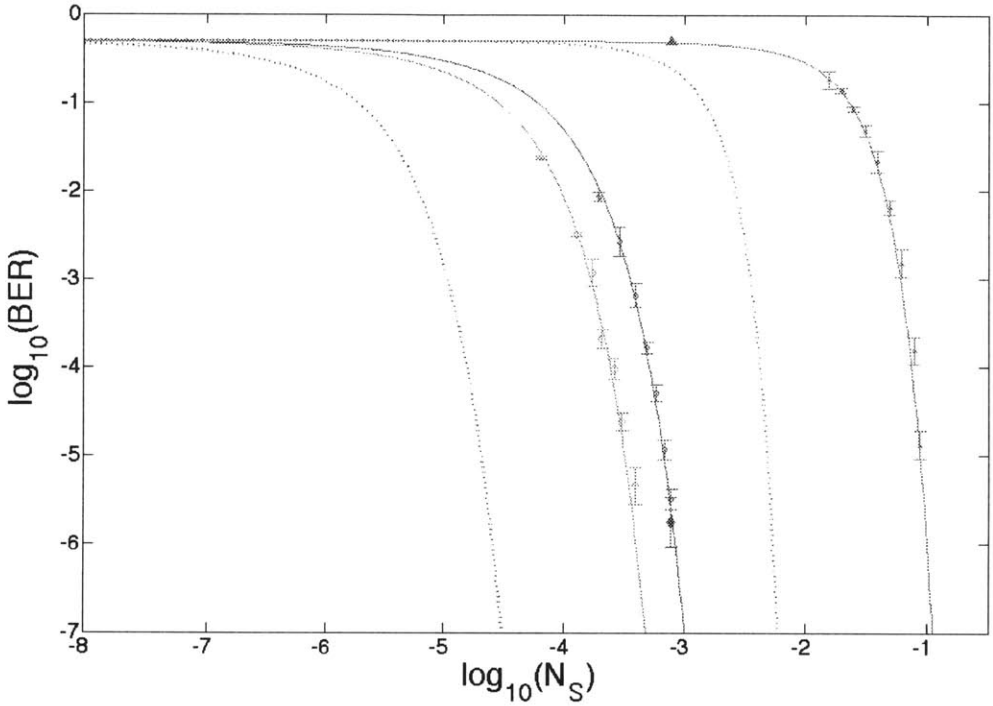

Figure 4-1: Plots of BER_A and BER_E as functions of source brightness N_S for 500 kbit/s communication. Red solid line: BER_A measured with a PiN diode. Other curves are the same as in Fig. 2-3.

For the experiment with the free-space channels, we have made a few changes shown in Table 2.1. The modifications are shown in Table 4.1.

4.2 Results of the Free-space Communication

The experimental measurements for the free-space Bob-to-Alice and Alice-to-Bob channels were done in the same way as described in chapter 2, except that we have decreased Bob's BPSK modulation rate to 180 kbit/s. The rate reduction was necessary because, given the simulated turbulence and uncompensated dispersion of the

Parameter	Symbol	Value
Bob's BPSK modulation rate	R	180 kbit/s
Bob's BPSK bit duration	T	5.56 μs
Alice's OPA gain - 1	G_A	1.8×10^{-4}
Alice's modulation-depth efficiency	η_d^A	0.18
Alice's number of mode pairs per T	M	1.11×10^7
Electronics-noise variance	σ_D^2	0.1

Table 4.1: Modifications in experimentally-determined parameter values for free-space QI-based communication.

additional fibers, the system could not be operated for long periods at the higher rates. As a consequence, the values for bit duration T and mode pairs per bit M have changed. In this experiment, Alice's modulation-depth efficiency η_d^A was reduced due to the additional uncompensated dispersion. The corresponding changes are listed in Table 4.1.

4.2.1 Analysis on the Bob-to-Alice Channel

We first replaced the free-space gap that was initially used for fine distance adjustment with a 1.2 m free-space channel. After we compensated the distance caused by insertion of the free-space channel on the idler side, we performed the BER measurement. The result is shown in Fig. 4-2.

Because the number of mode pairs per bit has increased from that of 500 kbit/s, Alice's and Eve's BER curves for ideal OPA receivers have shifted to the left compared to those at 500 kbit/s. For example, when N_S is 10^{-5}, Alice's calculated BER decreases from 1.5×10^{-3} (500 kbit/s) to 10^{-5} (180 kbit/s), which is almost two orders of magnitude decrease in error rate. However, the measured BER increased. For $N_S = 3.16 \times 10^{-4}$, Alice's BER increased from 1.11×10^{-5} (500 kbit/s) to 5.4×10^{-3} (180 kbit/s). This observed degradation in performance comes from the decrease in Alice's modulation-depth efficiency. However, in spite of Alice's performance degradation, Alice still can enjoy the advantage of quantum illumination for secure communication, because Eve's BER (not measured) is still much higher than Alice's. For $N_S = 3.16 \times 10^{-4}$, Eve's BER of her ideal receiver is approximately 32%,

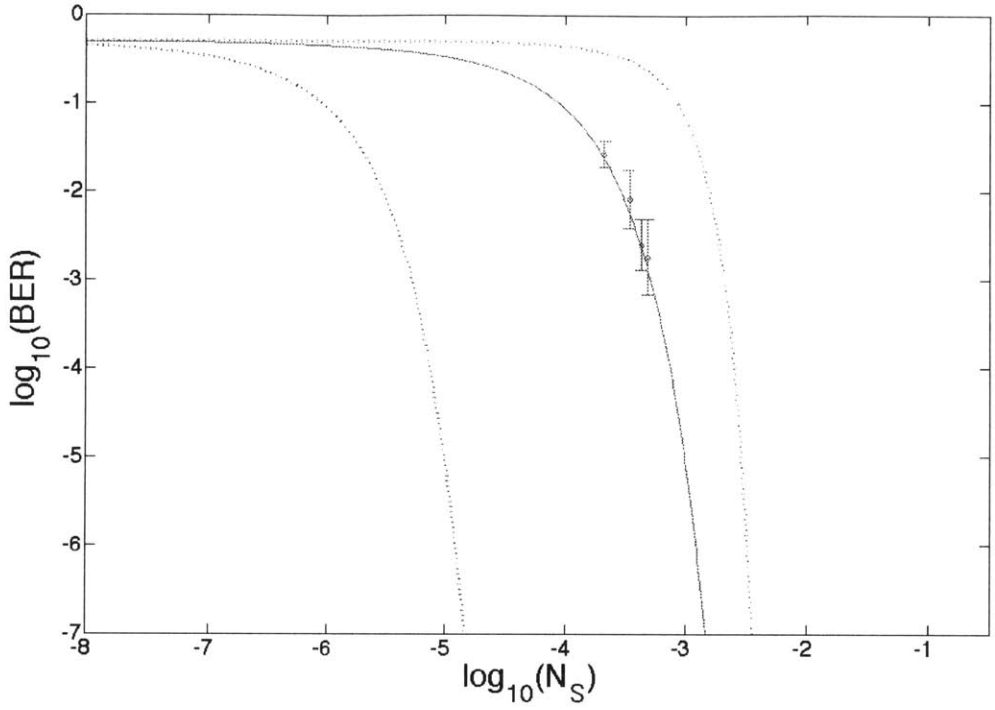

Figure 4-2: Plots of BER_A and BER_E as functions of source brightness N_S for 180 kbit/s communication when is replaced the Bob-to-Alice channel with a free-space channel. Blue-dotted line: BER_A for ideal OPA receiver; Blue solid line: BER_A for actual OPA receiver measured with a PiN diode; Red-dotted line: BER_E for ideal receiver.

which is about a thousand times greater than Alice's. Although the measurement of eavesdropping was not performed, we expect that Eve's eavesdropping performance would be much worse than her predicted BER for her ideal receiver.

Now, let us consider the effect of heat in the free-space channel. We do not currently model the effect of heat and relate it to the many studies of atmospheric turbulence [11]. Here we make a single assumption that the effect of heat decreases the fiber-coupled power that can lead to performance degradation. Let us denote $h(t)$ to be the attenuation factor caused by the heating plate. Note that $h(t)$ is a function of time, as the attenuation factor change over time. Moreover, we use this factor to account for other effects other than the power fluctuation. For example, when the signal beam is diffracted by air fluctuation, the amount of signal with the same phase may vary, thus causing an effective drop in power. Accurately modeling

of such effect is too complicated for this thesis work. For now, let us assume that $h(t)$ can represent all those unknown effects. In the current model, the transmissivity value for the Bob-to-Alice channel is κ_2. For modeling the effect of heat, we replace the Bob-to-Alice transmissivity κ_2 with κ_2'

$$\kappa_2' = h(t)\ \kappa_2. \tag{4.2}$$

This equation suggests that the Bob-to-Alice transmissivity is further attenuated by the effect of heat. From our analysis in chapter 3, we know that the effect of heat has a very low frequency range. From Fig. 3-10, we have observed that the effect is significant only under 25 Hz. This range is much lower than Bob's BPSK modulation rate (180 kbit/s). Hence, we can effectively replace the time-dependent attenuation factor $h(t)$ with a constant $\overline{h}$. The simplified Bob-to-Alice transmissivity becomes

$$\kappa_2' = \overline{h}\ \kappa_2. \tag{4.3}$$

When the servo system is in the closed-loop operation, we can minimize the effect of heat on the Bob-to-Alice transmissivity. As suggested in Fig. 3-9, the power fluctuation can be effectively suppressed using our feedback system. For the closed-loop operation, we can effectively neglect the effect of heat, and hence, the new Bob-to-Alice transmissivity can be assumed to be the same as the original

$$\kappa_2' = \kappa_2. \tag{4.4}$$

Fig. 4-3 shows Alice's calculated BER for the open-loop (black dashed) and closed-loop (blue solid) ($\overline{h} = 1$) operation. The open circle is the measured point for the open-loop operation, whereas the green filled diamond is the measured point for the closed-loop operation. By fitting the curves, we can extract the attenuation factor $\overline{h} \approx 0.63$. This value is smaller than the power measurements we observed in Fig. 3-9a. In the time trace plot of Fig.

3-9a, the power fluctuation does not drop by more than 20%. This suggests that the power fluctuation is not the only factor for the attenuation in the Bob-to-Alice

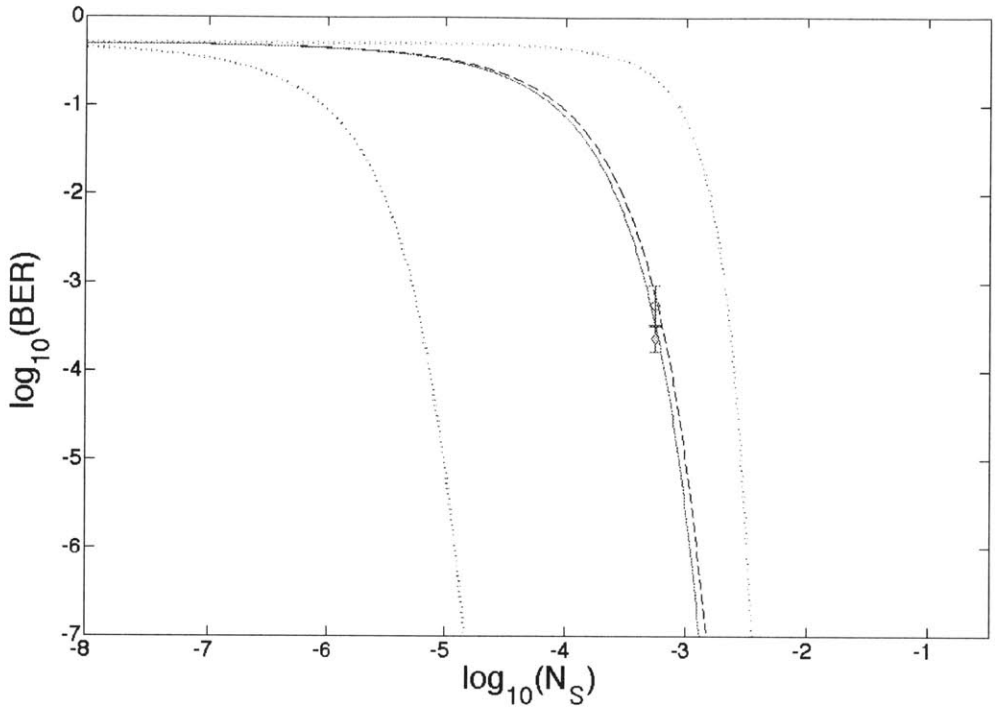

Figure 4-3: The effect of heat on the free-space Bob-to-Alice channel. Black dashed line: calculated open-loop operation with heat (open circle at measured point); Blue solid line: calculated closed-loop operation with heat (filled diamond at measured point).

effective transmissivity.

We can see that introducing heat in the Bob-to-Alice channel does not affect Alice's BER much. For $N_S \approx 5.59 \times 10^{-4}$, Alice's mean BER for the open-loop and closed-loop operations are 5.75×10^{-4} and 2.40×10^{-4}, respectively. The signal coming from Bob is already highly amplified by the EDFA. Hence, even if some loss is introduced over the channel, it does not affect the signal-to-noise ratio (SNR). Although the attenuation affects Alice's BER, it is not so critical.

4.2.2 Analysis on the Alice-to-Bob Channel

The measurement on the free-space Alice-to-Bob channel is done similarly to the Bob-to-Alice channel. First, we measured Alice's BER without introducing any heat in the channel. Because we have only replaced the location of the channel, the result

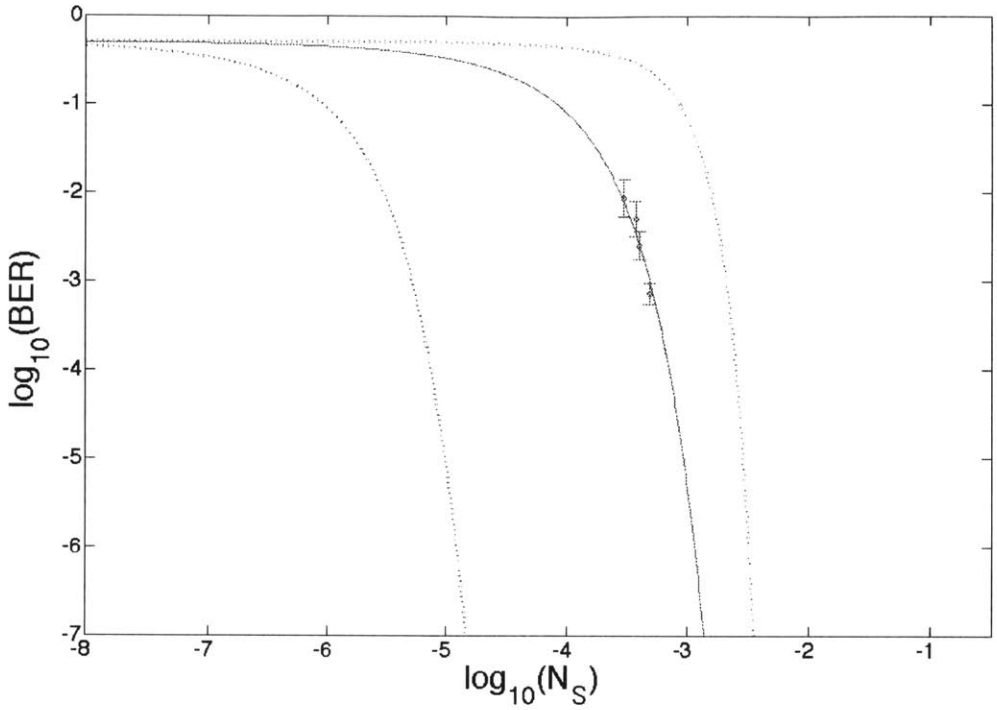

Figure 4-4: Plots of BER_A and BER_E as functions of source brightness N_S for 180 kbit/s communication when is replaced the Alice-to-Bob channel with a free-space channel. Blue-dotted line: BER_A for ideal OPA receiver; Blue solid line: BER_A for actual OPA receiver measured with a PiN diode; Red-dotted line: BER_E for ideal receiver.

must be the same as the Bob-to-Alice channel, and it is confirmed by Fig. 4-4.

Modeling the attenuation in the Alice-to-Bob channel can be done similarly as that for the Bob-to-Alice channel. For this case, we replace κ_1. For the open-loop operation,

$$\kappa_1' = \overline{h}\ \kappa_1, \tag{4.5}$$

and for the closed-loop operation,

$$\kappa_1' = \kappa_1. \tag{4.6}$$

Because we use the same heating plate setting for both Alice-to-Bob and Bob-to-Alice measurements, we expect that $\overline{h} \approx 0.63$. The experimental measurements are

shown in Fig. 4-5. Compared with the Bob-to-Alice case, we see that the same amount attenuation in the free-space channel affects the BER more severely in the Alice-to-Bob case. For $N_S \approx 5.58 \times 10^{-4}$, Alice's mean BER for the open-loop operation is 9.8×10^{-3}, and for the closed-loop operation, 4.90×10^{-4}. The gap between the open-loop and closed-loop operation is larger than that for the Bob-to-Alice measurement.

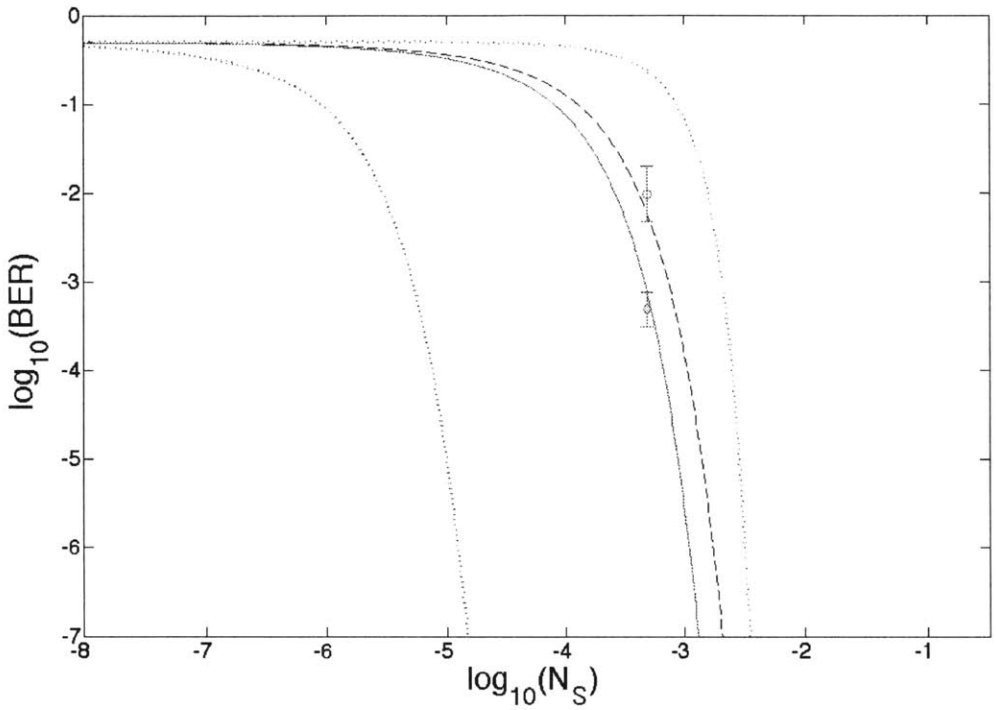

Figure 4-5: The effect of heat on the free-space Alice-to-Bob channel. Black dashed line: open-loop operation with heat (open circle at measured point); Blue solid line: closed-loop operation with heat (filled diamond with measured point).

From the theoretical model, we can understand why the free-space Alice-to-Bob channel suffers more from the effect of heat. If we lose the signal beam from the Alice-to-Bob channel, the number of signal photons that is encoded by the BPSK is reduced, and hence, the SNR for the Alice-to-Bob channel will be lowered. Such effect is undesirable for low BER. However, the Bob-to-Alice channel is different because it comes after the EDFA. The EDFA injects a large amount of noise to the signal beam and is the main source of noise, but it also amplifies the signal as well. Therefore, the SNR remains more or less the same with additional loss in this channel. There

is some information loss from the Bob-to-Alice channel due to heat, but it is not as critical as the loss in the Alice-to-Bob channel.

4.3 Further Experimental Optimization

There are more tasks to be done, because the experimental setup was not fully optimized. The first step is to compensate the dispersion effect. As mentioned previously, we did not compensate the dispersion effect at all for the insertion of a free-space channel. With the implementation of 1.2 m of free-space, we also implemented 4 meters of a normal single-mode fiber on the signal beam. A normal single-mode fiber has 17 ps of dispersion per bandwidth (nm) per length (km), where the bandwidth is given by the bandwidth of CWDM. Hence, the dispersion on the signal beam is

$$17 \text{ ps/nm/km} \times 16 \text{ nm} \times 0.004 \text{ km} = 1.09 \text{ ps}. \tag{4.7}$$

The amount of dispersion is large compared with the two-photon wavefunction time of 0.22 ps [9]. In order to compensate for the extra length on the idler side, we have implemented 7.11 m of a LEAF fiber, which has 4 ps of dispersion per bandwidth (nm) per length (km). For the idler, the dispersion effect is

$$6 \text{ ps/nm/km} \times 16 \text{ nm} \times 0.00711 \text{ km} = 0.455 \text{ ps}. \tag{4.8}$$

The sum of the dispersion effects is 1.56 ps. This effects can be compensated by insertion of 1 meter of dispersion compensating fiber (-120 ps/nm/km) to the signal side and 1 meter of LEAF fiber to the idler side. If the dispersion effect is compensated, we can expect an increase in Alice's modulation-depth efficiency and possibly allow us to increase the modulation rate.

We have often observed that the BER detector frequently lost synchronization with the lock-in amplifier during the measurement in the close-loop operation. The lock-in amplifier stabilizes the relative phases between the OPA pump, Alice's retained idler, and the modulated light she receives from Bob. Although the exact reason for

the lost synchronization is unknown, we need to fix this issue in order to make the system more robust. Although this needs to be verified, it might be caused by the piezoelectric mirror. During the closed-loop operation, the piezoelectric mirror tilts its angle very quickly to stablize the fiber coupling. However, the lock-in amplifier is only designed to stabilize small rapid changes in phase or slow large changes due to thermal fluctuation of the fibers. Our suspicion is a large-amplitude phase change introduced by the mirror is too fast for the lock-in amplifier, and that causes the BER detector to lose its synchronization. We have observed in time traces that show out-of-sync received signals with a π-phase shift relative to the message phase. This issue needs to be handled in order for higher rate and reliable operation.

Lastly, for this experiment, we have only implemented one piezoelectric mirror. For a longer distance communication and scenarios of more severe air turbulence, we need at least four degrees of freedom to correct the angle and the position of the beam. Study on how to implement more than one piezoelectric mirror needs to follow.

4.4 Conclusion

The previous QI-based secure communication using only a fiber channel shows that the QI protocol operates well in a noisy and lossy environment [9]. We have extended the fiber-based communication system to a free-space communication setup. In this experiment, we have demonstrated that the free-space secure communication using quantum illumination is still possible in an environment with air fluctuation by using a servo system to correct beam pointing deviations caused by air turbulence. Moreover, by analyzing the free-space Bob-to-Alice and Alice-to-Bob channels, we can also conclude that the implementation of the servo system is more crucial for the Alice-to-Bob channel.

Appendices

Appendix A

MATLAB Code for the free-space Alice-to-Bob Channel Analysis

I modified the code that was originally written by Zheshen Zhang. The function errorbar_tick can be found from MathWorks website.

```
clear all
close all

power_exp_openloop = 125/85*[85];
power0 = 200;

Ns_exp_openloop = power_exp_openloop/power0*7.81e-4;
lgNs_exp_openloop = log10(Ns_exp_openloop);

BER_exp_openloop = [1e-3*mean([3.2 4.2 10.6 9.6 8.5 11.0 20.1 ...
19.0 9.8 9.1 2.0])];

lgBER_exp_openloop = log10(BER_exp_openloop);

std_exp_openloop = [std(1e-3*[3.2 4.2 10.6 9.6 8.5 11.0 20.1 19.0 ...
```

```
9.8 9.1 2.0])];

lgstd_exp_openloop = [std(log10(1e-3*[3.2 4.2 10.6 9.6 8.5 11.0 20.1 ...
19.0 9.8 9.1 2.0]))];


power_exp_closedloop = 125/85*[85];
power0 = 200;

Ns_exp_closedloop = power_exp_closedloop/power0*7.81e-4;
lgNs_exp_closedloop = log10(Ns_exp_closedloop);

BER_exp_closedloop = [1e-4*mean([4.00 3.3 6.00 3.00 2.01 4.00 4.06 ...
4.6 8.71 9.03 5.00])];

lgBER_exp_closedloop = log10(BER_exp_closedloop);

std_exp_closedloop = [std(1e-4*[4.00 3.3 6.00 3.00 2.01 4.00 4.06 4.6 8.71 ...
9.03 5.00])];

lgstd_exp_closedloop = [std(log10(1e-4*[4.00 3.3 6.00 3.00 2.01 4.00 4.06 ...
4.6 8.71 9.03 5.00]))];

%%%%%%%%%%%%%%%%%%%%%%%%%%%%%%%%%%%%

kappa_I = 0.39;
kappa_1 = 0.5;
kappa_2 = 0.9;

kappa_GA = 0.74;
kappa_GB = 0.4324;
```

```
kappa_BB = 0.39;
kappa_BA = 0.4084;

kappa_GE = 1;
kappa_BE = 0.013;

GOPA = 1.00018;
kappa_E = 0.99;

P_EDFA = 3.5e-3; % for one polarization
Optical_BW = 2e12; % bandwidth of the down-converted light is 2 THz
E = 0.8*1.6e-19; % photon energy at 1550 nm
N_S = logspace(-8,0,1000);
lgN_S = log10(N_S);
BitRate = 180e3; % transmission bit rate
T = 1/BitRate; % observation time of one bit
M = Optical_BW*T;
GAPD = 6.7; % gain of the APD at 57 V bias voltage
GAMP = 1e7; % gain of the electronic amplifier after the APD
GE = GAPD*GAMP; % gain of Eve's detector
QE = 0.7*0.8*0.8;

FdB = 3.4;
F = 10^(.1*FdB);

%N_B = P_EDFA/Optical_BW/E;
N_B = 10^-.427/125e9/E/1000/2/.8;

GEDFA = (2*N_B+1)/F;

eta_d = 0.19;
eta_d_E = .17;
```

```
var_elec_noise_PM = 0.1; %0.042;

r = 0.2;
r_E = 2; %  Eve's total noise is F*sigma^2_E

%%%%%%%%%%%%%%%%%%%%%%%%%%%%%%%%%%%%%

NA0_PM = GOPA*kappa_I*N_S+(GOPA-1)*kappa_GA*kappa_1*kappa_GB*kappa_BB ...
*kappa_2*kappa_BA*GEDFA*N_S+(GOPA-1)*kappa_2*kappa_BB ...
*kappa_BA*N_B+(GOPA-1)+2*eta_d*sqrt(GOPA*(GOPA-1)*kappa_I ...
*kappa_GA*kappa_GB*kappa_BB*kappa_BA*kappa_1 ...
*GEDFA*N_S.*(N_S+1)*kappa_2);
% Alice's average photon number per mode for bit 0
NA1_PM = GOPA*kappa_I*N_S+(GOPA-1)*kappa_GA*kappa_1*kappa_GB*kappa_BB ...
*kappa_2*kappa_BA*GEDFA*N_S+(GOPA-1)*kappa_2*kappa_BB ...
*kappa_BA*N_B+(GOPA-1)-2*eta_d*sqrt(GOPA*(GOPA-1)*kappa_I ...
*kappa_GA*kappa_GB*kappa_BB*kappa_BA*kappa_1 ...
*GEDFA*N_S.*(N_S+1)*kappa_2);
% Alice's average photon number per mode for bit 1

NA0_PM = NA0_PM*QE;
NA1_PM = NA1_PM*QE;

var_NA0_PM = NA0_PM.*(NA0_PM+1);
var_NA1_PM = NA1_PM.*(NA1_PM+1);

var_pump_noise = var_NA0_PM*r;

sigma_NA0_tot = sqrt(var_elec_noise_PM+(r+1)*var_NA0_PM);
sigma_NA1_tot = sqrt(var_elec_noise_PM+(r+1)*var_NA1_PM);
```

```
sigma_NA_tot = 1/2*(sigma_NA0_tot+sigma_NA1_tot);


BER_Alice_th = qfunc(sqrt(M)*(NA0_PM-NA1_PM)/2./sigma_NA_tot);
lgBER_Alice_th = log10(BER_Alice_th);

%%%%%%%%%%%%%%%%%%%%%%%%%%%%%%%%%%%%

NA0_PM_ideal = GOPA*kappa_I*N_S+(GOPA-1)*kappa_GA*kappa_1*kappa_GB*kappa_BB ...
*kappa_2*kappa_BA*GEDFA*N_S+(GOPA-1)*kappa_2*kappa_BB ...
*kappa_BA*N_B+(GOPA-1)+2*sqrt(GOPA*(GOPA-1)*kappa_I ...
*kappa_GA*kappa_GB*kappa_BB*kappa_BA*kappa_1 ...
*GEDFA*N_S.*(N_S+1)*kappa_2);
% Alice's average photon number per mode for bit 0
NA1_PM_ideal = GOPA*kappa_I*N_S+(GOPA-1)*kappa_GA*kappa_1*kappa_GB*kappa_BB ...
*kappa_2*kappa_BA*GEDFA*N_S+(GOPA-1)*kappa_2*kappa_BB ...
*kappa_BA*N_B+(GOPA-1)-2*sqrt(GOPA*(GOPA-1)*kappa_I ...
*kappa_GA*kappa_GB*kappa_BB*kappa_BA*kappa_1 ...
*GEDFA*N_S.*(N_S+1)*kappa_2);
% Alice's average photon number per mode for bit 1


var_NA0_PM_ideal = NA0_PM_ideal.*(NA0_PM_ideal+1);
var_NA1_PM_ideal = NA1_PM_ideal.*(NA1_PM_ideal+1);


sigma_NA0_tot_ideal = sqrt(var_NA0_PM_ideal);
sigma_NA1_tot_ideal = sqrt(var_NA1_PM_ideal);

sigma_NA_tot_ideal = 1/2*(sigma_NA0_tot_ideal+sigma_NA1_tot_ideal);
```

```
BER_Alice_ideal = qfunc(sqrt(M)*(NA0_PM_ideal-NA1_PM_ideal)/2./sigma_NA_tot_ideal);
lgBER_Alice_ideal = log10(BER_Alice_ideal);

%%%%%%%%%%%%%%%%%%%%%%%%%%%%%%%%%%%%

NE0_PM_ideal = kappa_E*kappa_GA*(1-kappa_1)*kappa_GE*N_S+(1-kappa_E) ...
*(1-kappa_2)*kappa_BB*GEDFA*kappa_1*kappa_GA*kappa_GB ...
*kappa_BE*N_S+(1-kappa_E)*(1-kappa_2)*kappa_BB*kappa_BE ...
*N_B+2*sqrt(kappa_E*(1-kappa_E)*(1-kappa_1)*(1-kappa_2) ...
*kappa_GA^2*kappa_GB*kappa_BB*GEDFA*kappa_1 ...
*kappa_GE*kappa_BE)*N_S;
% Eve's average photon number per mode for bit 0
NE1_PM_ideal = kappa_E*kappa_GA*(1-kappa_1)*kappa_GE*N_S+(1-kappa_E) ...
*(1-kappa_2)*kappa_BB*GEDFA*kappa_1*kappa_GA*kappa_GB ...
*kappa_BE*N_S+(1-kappa_E)*(1-kappa_2)*kappa_BB*kappa_BE ...
*N_B-2*sqrt(kappa_E*(1-kappa_E)*(1-kappa_1)*(1-kappa_2) ...
*kappa_GA^2*kappa_GB*kappa_BB*GEDFA*kappa_1 ...
*kappa_GE*kappa_BE)*N_S;
% Eve's average photon number per mode for bit 1

var_NE0_PM_ideal = NE0_PM_ideal.*(NE0_PM_ideal+1);
var_NE1_PM_ideal = NE1_PM_ideal.*(NE1_PM_ideal+1);

sigma_E_ideal = 1/2*(sqrt(var_NE0_PM_ideal)+sqrt(var_NE1_PM_ideal));

BER_Eve_ideal = qfunc(sqrt(M)*(NE0_PM_ideal-NE1_PM_ideal)/2./sigma_E_ideal);
lgBER_Eve_ideal = log10(BER_Eve_ideal);

%%%%%%%%%%%%%%%%%%%%%%%%%%%%%%%%%%%%

A = 0.63; % attenuation
```

```
kappa_1 = A * 0.5;

NA0_PM_heat = GOPA*kappa_I*N_S+(GOPA-1)*kappa_GA*kappa_1*kappa_GB*kappa_BB ...
*kappa_2*kappa_BA*GEDFA*N_S+(GOPA-1)*kappa_2*kappa_BB ...
*kappa_BA*N_B+(GOPA-1)+2*eta_d*sqrt(GOPA*(GOPA-1)*kappa_I ...
*kappa_GA*kappa_GB*kappa_BB*kappa_BA*kappa_1 ...
*GEDFA*N_S.*(N_S+1)*kappa_2);
% Alice's average photon number per mode for bit 0
NA1_PM_heat = GOPA*kappa_I*N_S+(GOPA-1)*kappa_GA*kappa_1*kappa_GB*kappa_BB ...
*kappa_2*kappa_BA*GEDFA*N_S+(GOPA-1)*kappa_2*kappa_BB ...
*kappa_BA*N_B+(GOPA-1)-2*eta_d*sqrt(GOPA*(GOPA-1)*kappa_I ...
*kappa_GA*kappa_GB*kappa_BB*kappa_BA*kappa_1 ...
*GEDFA*N_S.*(N_S+1)*kappa_2);
% Alice's average photon number per mode for bit 1

NA0_PM_heat = NA0_PM_heat*QE;
NA1_PM_heat = NA1_PM_heat*QE;

var_NA0_PM_heat = NA0_PM_heat.*(NA0_PM_heat+1);
var_NA1_PM_heat = NA1_PM_heat.*(NA1_PM_heat+1);

var_pump_noise = var_NA0_PM_heat*r;

sigma_NA0_tot_heat = sqrt(var_elec_noise_PM+(r+1)*var_NA0_PM_heat);
sigma_NA1_tot_heat = sqrt(var_elec_noise_PM+(r+1)*var_NA1_PM_heat);

sigma_NA_tot_heat = 1/2*(sigma_NA0_tot_heat+sigma_NA1_tot_heat);


BER_Alice_th_heat = qfunc(sqrt(M)*(NA0_PM_heat-NA1_PM_heat)/2./sigma_NA_tot_heat);
lgBER_Alice_th_heat = log10(BER_Alice_th_heat);
```

```
%%%%%%%%%%%%%%%%%%%%%%%%%%%%%%%%%%
%loglog(N_S,BER_Alice_th);
%axis([min(N_S) max(N_S) 10^-7 10^0])

figure
h_A = plot(lgN_S,lgBER_Alice_ideal,'b:',lgN_S,lgBER_Eve_ideal,'r:', ...
lgN_S,lgBER_Alice_th_heat,'k--');
hold on;
h_A_th = plot(lgN_S,log10(BER_Alice_th),'b');

h_openloop = errorbar(lgNs_exp_openloop,lgBER_exp_openloop,lgstd_exp_openloop,'o');
errorbar_tick(h_openloop,0.1,'UNITS');

h_closedloop = errorbar(lgNs_exp_closedloop,lgBER_exp_closedloop, ...
lgstd_exp_closedloop,'d','MarkerFaceColor','g');
errorbar_tick(h_closedloop,0.1,'UNITS');

axis([-8 -0.5 -7 0])

xlabel('log_{10}(N_S)','Fontsize',30)
ylabel('log_{10}(BER)','Fontsize',30)

set(gca,'Fontsize',20);
set(h_A,'Linewidth',1);
set(h_A,'Markersize',15);
set(h_openloop,'Markersize',8);
set(h_openloop,'Linewidth',1);
set(h_closedloop,'Markersize',8);
set(h_closedloop,'Linewidth',1);

print(gcf,'-depsc','BER_vs_pumppower_loglog.eps')
```

Bibliography

[1] Seth Lloyd. Enhanced sensitivity of photodetection via quantum illumination. *Science*, 321:1463-1465, 2008.

[2] Thomas Jennewein, Christoph Simon, Gregor Weihs, Harald Weinfurter, and Anton Zeilinger. Quantum cryptography with entangled photons. *Phys. Rev. Lett.*, 84:4729-4732, May 2000.

[3] Peter W. Shor. Polynomial-time algorithms for prime factorization and discrete logarithms on a quantum computer. *SIAM J. Comput.*, 26(5):1484-1509, 1997.

[4] Vittorio Giovannetti, Seth Lloyd, and Lorenzo Maccone. Quantum-enhanced measurements: Beating the standard quantum limit. *Science*, 306(5700):1330-1336, 2004.

[5] Si-Hui Tan, Baris Erkmen, Vittorio Giovannetti, Saikat Guha, Seth Lloyd, Lorenzo Maccone, Stefano Pirandola, and Jeffrey H. Shapiro. Quantum illumination with gaussian states. *Phys. Rev. Lett.*, 101:253601, 2008.

[6] Jeffrey H. Shapiro and Seth Lloyd. Quantum illumination versus coherent-state target detection. *New Journal of Physics*, 11(6):063045-060349, 2009.

[7] J.H. Shapiro, Defeating passive eavesdropping with quantum illumination. *Phys. Rev. A*, 80, 022320 (2009).

[8] E. D. Lopaeva, I. Ruo Berchera, I. P. Degiovanni, S. Olivares, G. Brida, and M. Genovese. Experimental realisation of quantum illumination. *Phys. Rev. Lett.*, 110, 153603, April 2013.

[9] Zheshen Zhang, Maria Tengner, Tian Zhong, Franco N. C. Wong, and Jeffrey H. Shapiro. Entanglement's benefit survives an entanglement-breaking channel. *Phys. Rev. Lett.*, 111, 010501, July 2013.

[10] M. M. Fejer, G. A. Magel, D. H. Jundt, and R. L. Byer, Quasi-phase-matched second harmonic generation: tuning and tolerances. IEEE J. Quantum Electron. 28, 2631 (1992).

[11] J.H. Shapiro, Near-field turbulence effects on quantum-key distribution. *Phys. Rev. A*, 67, 022309 (2003).